

Cross sections for nuclide production in 1 GeV proton-irradiated ^{208}Pb

Yu. E. Titarenko, O. V. Shvedov, V. F. Batyaev, E. I. Karpikhin, V. M. Zhivun,
A. B. Koldobsky, R. D. Mulambetov, D. V. Fischenko, S. V. Kvasova, A. N. Sosnin
*Institute for Theoretical and Experimental Physics, B.Cheremushkinskaya 25,
117259 Moscow, Russia*

S. G. Mashnik, R. E. Prael, A. J. Sierk
Los Alamos National Laboratory, Los Alamos, NM 87545, USA

T. A. Gabriel
Oak Ridge National Laboratory, Oak Ridge, TN 37831, USA

M. Saito
Tokyo Institute of Technology 2-12-1, O-okayama, Meguro-ku, Tokyo 152, Japan

H. Yasuda
*Japan Atomic Energy Research Institute, Tokai, Ibaraki, 319-1195, Japan
(October 30, 2018)*

114 cross sections for nuclide production in a 1.0 GeV proton-irradiated thin ^{208}Pb target have been measured by the direct γ -spectrometry method using a high-resolution Ge detector. The γ spectra were processed by the GENIE-2000 code. The ITEP-developed SIGMA code was used together with the PCNUDAT nuclear decay database to identify the γ lines and to determine the cross sections. The $^{27}\text{Al}(p,x)^{22}\text{Na}$ reaction was used to monitor the proton flux. Results of a feasibility study of the auxiliary $^{27}\text{Al}(p,x)^{24}\text{Na}$ and $^{27}\text{Al}(p,x)^7\text{Be}$ monitor reactions in the 0.07–2.6 GeV proton-energy range are presented as well. Most of the experimental data have been analyzed by the LAHET (with ISABEL and Bertini options), CEM95, CEM2k, INUCL, CASCADE, CASCADE/INPE, and YIELDX codes that simulate hadron-nucleus interactions.

25.40.Sc, 24.10.-i, 29.30.Kv, 29.85.+c

I. INTRODUCTION

Major advances in Pb-Bi reactor technology, as manifested in the Russian-made Alpha-class submarines, has made Pb-Bi technology attractive for accelerator-driven systems (ADS) to be used at facilities designed to transmute nuclear waste [1–3]. These Pb-Bi reactors would operate in an environment of high-energy radiation, thus motivating studies of the nucleonics characteristics of lead and bismuth, including the yields of residual product nuclei under irradiation by protons of energies ranging from a few MeV to 2–3 GeV. Results of such studies are extremely important when designing even demonstration versions of ADS facilities. Yields of residual product nuclei define important characteristics of these facilities such as radioactivity (both current and residual), deterioration of corrosion resistance, yields of gaseous products, neutron “poisoning”, etc. That is why several scientific groups have been studying the yields of residual product nuclei from Pb and Bi (both natural and isotope-enriched) bombarded with protons in the desired energy range [4–10].

Most of these studies have been made using γ spectrometry on proton-irradiated natural or monoisotopic thin Pb and Bi samples (for example, $p+^{208}\text{Pb}$). This technique makes it possible to determine the independent

and cumulative yields of more than a hundred reaction products [4–7]. An alternative technique of magnetically separating the reaction products after a heavy-ion beam interacts with a liquid H target, using reverse kinematics, as done recently at GSI to study ^{238}U , ^{197}Au and $^{208}\text{Pb}+^1_1\text{H}$, makes it possible to determine about a thousand yields [8–10].

Comparing the results of the two techniques helps in understanding the systematic errors inherent to both. This work makes use of the γ -spectrometry technique. We discuss below our results as well as the systematic errors of γ spectrometry.

Necessarily, computational methods will play an important role in the designs for ADS facilities. Therefore, testing of the most extensively used simulation codes is necessary. We perform a qualitative and quantitative comparison of our data with simulated results from seven codes widely used in applications.

II. BASIC DEFINITIONS AND FORMULAS

The formalism for finding the reaction product yields (cross sections) in high-energy proton-irradiated thin targets is described in sufficient detail in [6]. Any of the measured reaction products generated in nucleon interactions with matter are assumed to originate both

in the reaction proper and in the decays of its chain precursors. Thus, the set of terms invented earlier in studying the mass and charge distributions of fission products (see, e. g., [11]) can conveniently be used when processing and interpreting the experimental results of the present work. In this terminology, the independent and cumulative yields of products underlie the formalism.

The independent yield of a reaction product nuclide is a cross section for the nuclide to be produced directly in the reaction, whereas the cumulative yield of the nuclide is a cross section for the nuclide to be produced in all the appropriate processes, i.e., both directly in the reaction and over the time during the decays of all of its chain precursors.*

The variations in the concentration of any two nuclides of a chain produced in an irradiated target ($N_1 \xrightarrow{\lambda_1} N_2 \xrightarrow{\lambda_2}$) may be modeled as a set of differential equations that describe the production and decays of the nuclides. By introducing the time functions, F_i , of the type $F_i = (1 - e^{-\lambda_i \tau}) \frac{1 - e^{-\lambda_i K T}}{1 - e^{-\lambda_i T}}$, ($i = 1, 2$, or monitor product (Na or another)); τ is the duration of a single proton pulse, T is the pulse repetition period, K is the number of irradiation pulses which characterize the nuclide decays within the irradiation time, and by expressing (similar to the relative measurements) the proton fluence via the monitor reaction cross section σ_{st} , we can present the cumulative and independent yields as

$$\sigma_1^{cum} = \frac{A_0}{\eta_1 \varepsilon_1 F_1 N_{Na}} \frac{N_{Al} F_{Na}}{N_T \lambda_{Na}} \sigma_{st}, \quad (1)$$

or, if measurements of the second nuclide alone are used, as

$$\sigma_1^{cum} = \frac{A_1}{\nu_1 \eta_2 \varepsilon_2 F_1 N_{Na}} \frac{N_{Al} \lambda_2 - \lambda_1 F_{Na}}{N_T \lambda_2 \lambda_{Na}} \sigma_{st}, \quad (2)$$

$$\sigma_2^{ind} = \left(\frac{A_2}{F_2} + \frac{A_1 \lambda_1}{F_1 \lambda_2} \right) \frac{1}{\eta_2 \varepsilon_2 N_{Na}} \frac{N_{Al} F_{Na}}{N_T \lambda_{Na}} \sigma_{st}, \quad (3)$$

$$\begin{aligned} \sigma_2^{cum} &= \sigma_2^{ind} + \nu_1 \sigma_1^{cum} = \\ &= \left(\frac{A_1}{F_1} + \frac{A_2}{F_2} \right) \frac{1}{\eta_2 \varepsilon_2 N_{Na}} \frac{N_{Al} F_{Na}}{N_T \lambda_{Na}} \sigma_{st}. \end{aligned} \quad (4)$$

Here, σ_1^{cum} is the cumulative [†] cross section of the first nuclide N_1 ; σ_2^{ind} and σ_2^{cum} are the independent and cumulative cross sections of the second nuclide N_2 ; N_{Al}

and N_T are the numbers of nuclei in the monitor and in the experimental target, respectively; N_{Na} is the number of Na nuclei produced in the monitor; η_1 and η_2 are γ -line yields; ε_1 and ε_2 are the spectrometer efficiencies at energies E_{γ_1} and E_{γ_2} ; ν_1 is the branching ratio of the first nuclide; λ_1 , λ_2 , and λ_{Na} are, respectively, the decay constants of the first and second nuclides and of the monitor product (^{22}Na and/or ^{24}Na).

The factors A_0 , A_1 , and A_2 are calculated through fitting the measured counting rates in the total absorption peaks, which correspond to energies E_{γ_1} (the first nuclide) and E_{γ_2} (the second nuclide), by the exponential functions

$$g(t) = A_0 \frac{1 - e^{-\lambda_1 t_{true}}}{\lambda_1 t_{true}} e^{-\lambda_1 t} \quad (5)$$

and

$$\begin{aligned} f(t) &= A_1 \frac{1 - e^{-\lambda_1 t_{true}}}{\lambda_1 t_{true}} e^{-\lambda_1 t} + \\ &+ A_2 \frac{1 - e^{-\lambda_2 t_{true}}}{\lambda_2 t_{true}} e^{-\lambda_2 t}. \end{aligned} \quad (6)$$

Here, t_{true} is the real time over which the spectrum is measured, t is the time between the end of the irradiation and the beginning of the spectrum measurement. The forms of functions (5) and (6) are similar to what is presented in [6], but we present them here for clarity:

$$A_0 = N_T \Phi \sigma_1^{cum} \eta_1 \varepsilon_1 F_1, \quad (7)$$

$$A_1 = N_T \Phi \sigma_1^{cum} \eta_2 \varepsilon_2 F_1 \nu_1 \lambda_2 / (\lambda_2 - \lambda_1), \quad (8)$$

$$A_2 = N_T \Phi \eta_2 F_2 [\sigma_2^{ind} - \sigma_1^{cum} \nu_1 \lambda_1 / (\lambda_2 - \lambda_1)]. \quad (9)$$

It should be noted that formulas (1)–(4) are deduced on the assumption that the corresponding γ counting rates of each nuclide produced under irradiation are determined to within the desired accuracy throughout the time interval from the irradiation end to the ultimate intensity detection threshold. Curve 1 of Fig. 1 exemplifies such a favorable situation. The situation corresponds to the ^{192}Hg ($T_{1/2} = 4.85$ hours) \rightarrow ^{192}Au ($T_{1/2} = 4.94$ hours) decay chain, with the ^{192}Au , 316.5 keV γ line being measured. Despite the very similar periods, the absence of any addends to the measured γ line (i.e., null contribution from γ lines of any other nuclides whose energy is the same, within the spectrometer resolution, as of the measured γ line) provides a sufficiently accurate determination of the cumulative ^{192}Hg yield, as well as the independent and cumulative ^{192}Au yields.

The real situation often gets more complicated, however, because the decay curve of the second nuclide cannot be measured correctly in every case within the desired (in the sense as mentioned above) time interval. Its γ -line intensity is often difficult to measure in the beginning of a measurement run, right after the irradiation stops. In the case of short-lived nuclides, this is due to the fact that within the period from the end of irradiation to

*Some applications also make use of the mass yield. In its simplified form (disregarding alpha transitions and delayed-neutron emission), the mass yield is the sum of all independent yields of the isobars of a given mass or equivalently is the sum of cumulative yields of the stable isotopes of a given mass.

[†]In case of absence of short-lived precursors, the yield of the nuclide N_1 should be considered as independent.

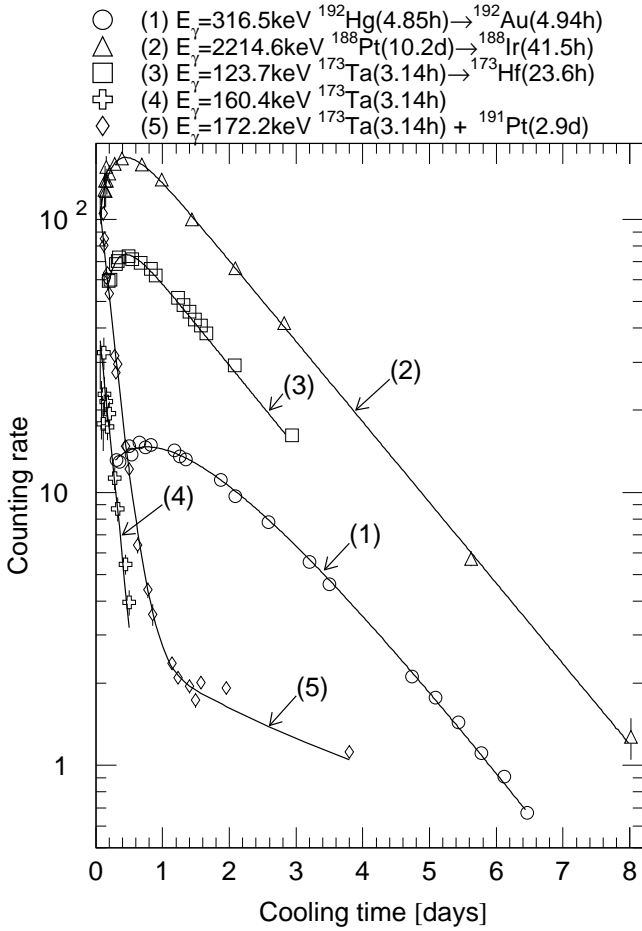


FIG. 1. Typical examples of decay curves. Curve (1) is for the chain $^{192}\text{Hg} \rightarrow ^{192}\text{Au}$. Curve (2) is for $^{188}\text{Pt} \rightarrow ^{188}\text{Ir}$. Curve (3) is for $^{173}\text{Ta} \rightarrow ^{173}\text{Hf}$. Curve (4) is for the independent ^{173}Ta decay. Curve (5) is for the independent ($^{173}\text{Ta} + ^{191}\text{Pt}$) decay. Curve (1) is drawn with a time scale factor of 4 and a counting rate factor of 0.1. Curve (2) is drawn with a time scale factor of 0.1 and a counting rate factor of 100.

the beginning of a measurement run (the cooling time), the nuclide N_1 (precursor) can partly or fully decay (if $\lambda_1 > \lambda_2$), or else a full or partial equilibrium sets in (if $\lambda_1 < \lambda_2$) between the nuclides N_1 and N_2 .

The contribution from nuclide N_1 will then never be reflected in the experimental decay curve of nuclide N_2 . The situation gets even more complicated because a great number of the products can include nuclides whose half-lives are close to the half-life of a shorter-lived nuclide, either N_1 or N_2 . In that case, as noted above, if the γ -line energy of such nuclides is the same (within the spectrometer resolution) as the measured γ -line energy of other nuclide, then neither of the factors A_1 and A_2 can be determined, or else the two can only be determined with great uncertainty and thus become useless for calculating the yields.

Fig. 1 is also a good illustration of a possible unfa-

vorable situation for analyzing the nuclides of similar half-lives (Curve 1). If the ^{192}Au decay curve begins being measured more than two days after the irradiation, the ^{192}Hg contribution becomes uncertain, resulting in erroneous calculations of the ^{192}Au yield. Such a situation is most probably responsible for the difference in the measured ^{192}Au yields of more than a factor 3 between the data of the present work (see Table II below) and the results of [4] (46.9 ± 6.6 mb and 160 ± 50 mb, respectively).

Analyzing possible structures of radioactive chains permits the following two very common situations to be singled out.

First, assume that $\lambda_1 < \lambda_2$. This situation is exemplified in Fig. 1 (Curve 2), which shows the decay curve of chain nuclides $^{188}\text{Pt} (T_{1/2}=10.2 \text{ days}) \rightarrow ^{188}\text{Ir} (T_{1/2}=41.5 \text{ hours})$ recorded by measuring the 2214.6 keV γ line of the ^{188}Ir daughter nuclide. In this case, the decay curve of nuclide ^{188}Ir can be used to obtain fairly accurate values of the factors A_1 and A_2 and, hence, of σ_1^{cum} , σ_2^{ind} , and σ_2^{cum} ($\sigma_{^{188}\text{Pt}}^{cum}$, $\sigma_{^{188}\text{Ir}}^{ind}$, and $\sigma_{^{188}\text{Ir}}^{cum}$). Should this favorable situation get complicated (for example, the measurements began in 2 days after irradiation), then, even without observing the knee, the conclusion concerning the ^{188}Pt production is quite obvious because the 2214.6 keV γ line of ^{188}Ir is measured with the ^{188}Pt period. In this case, formula (2) may be used to calculate the $\sigma_{^{188}\text{Pt}}^{cum}$ value, whereas the ^{188}Ir data prove to be lost.

It should be noted that there even exists a nuclear data library that presents the ^{188}Pt gamma yields corrected for the $(\lambda_2 - \lambda_1)/\lambda_2$ value. The corrected yields are marked with an index (D) to notify the validity of using the daughter nuclide γ lines when calculating the number of mother nuclei [12].

The inverse situation ($\lambda_1 > \lambda_2$) permits the factor A_2 alone to be determined reliably. This is exemplified by Curve 3 in Fig. 1, which is the decay curve of the chain nuclides $^{173}\text{Ta} (T_{1/2}=3.14 \text{ hours}) \rightarrow ^{173}\text{Hf} (T_{1/2}=23.6 \text{ hours})$ recorded by measuring the 123.7 keV γ line of ^{173}Hf . In this case, the factors A_1 and A_2 can be determined to within the desired accuracy, and formulas (2)–(4) can be used to calculate σ_1^{cum} , σ_2^{ind} , and σ_2^{cum} ($\sigma_{^{173}\text{Ta}}^{cum}$, $\sigma_{^{173}\text{Hf}}^{ind}$, and $\sigma_{^{173}\text{Hf}}^{cum}$). In cases when unfavorable situations arise due to, for example, measurements starting a day after the irradiation, the factor A_1 alone can be determined.

If, however, the eigen γ line is used (this is shown in Fig. 1 by Curve 4, which is the ^{173}Ta decay curve measured by the 160.4 keV ^{173}Ta γ line, or by Curve 5, which is the same, but inferred from the 172.3 keV ^{173}Ta γ line with an addend contributed by the ^{191}Pt decay), then the factor A_0 can be calculated and the missing factor A_1 is

$$A_1 = A_0 \frac{\eta_2 \varepsilon_2}{\eta_1 \varepsilon_1} \nu_1 \frac{\lambda_2}{\lambda_2 - \lambda_1}, \quad (10)$$

whereupon formulas (2)–(4) can be used to find σ_1^{cum} , σ_2^{ind} , and σ_2^{cum} ($\sigma_{^{173}\text{Ta}}^{cum}$, $\sigma_{^{173}\text{Hf}}^{ind}$, and $\sigma_{^{173}\text{Hf}}^{cum}$). If, however,

the factor A_1 cannot be found, we may use the factor A_2 together with expression (14) from [6] to determine the quantity σ_2^{cum*} , which we call the supra cumulative yield:

$$\begin{aligned}\sigma_2^{cum*} &= \sigma_2^{ind} + \frac{\lambda_1}{\lambda_1 - \lambda_2} \nu_1 \sigma_1^{cum} = \\ &= \frac{A_2}{\eta_2 \varepsilon_2 F_2 N_{Na}} \frac{N_{Al}}{N_T} \frac{F_{Na}}{\lambda_{Na}} \sigma_{st} .\end{aligned}\quad (11)$$

It should be noted that the difference between σ_2^{cum} and σ_2^{cum*} is not specified in many of the relevant publications despite the fact that σ_2^{cum*} is always greater than σ_2^{cum} . The explanation is that the formal equality $\sigma_2^{cum} = \sigma_2^{cum*}$ holds in case the generation times of the first and second nuclides are different. In this case, the time correction can be determined:

$$\Delta t = \frac{1}{\lambda_2} \left[1 + \frac{\nu_1 \sigma_1^{cum}}{\sigma_2^{ind} + \nu_1 \sigma_1^{cum}} \left(\frac{\lambda_2}{\lambda_1 - \lambda_2} \right) \right]. \quad (12)$$

From formula (12), it is seen that Δt depends on the yields σ_1^{cum} and σ_2^{ind} , thereby preventing the time correction Δt from being allowed for in a general case when determining σ_2^{cum} . In common cases of $\sigma_2^{ind} \ll \nu_1 \sigma_1^{cum}$, however, the time correction Δt can be shown to depend on the decay constants only:

$$\Delta t \cong \Delta t' = \frac{1}{\lambda_2} \left[1 + \left(\frac{\lambda_2}{\lambda_1 - \lambda_2} \right) \right]. \quad (13)$$

Therefore, the cumulative yield of the second nuclide can be determined after a post-irradiation period sufficient for N_1 to decay into N_2 (normally, this equals from 6 to 10 half-lives of the first nuclide) by measuring the decay curve of the first nuclide making allowance for the time correction Δt :

$$\begin{aligned}\sigma_2^{cum} &= \frac{A_2}{\eta_2 \varepsilon_2 F_2 N_{Na}} \frac{N_{Al}}{N_T} \frac{F_{Na}}{\lambda_{Na}} \sigma_{st} e^{-\lambda_2 \Delta t} \cong \\ &\cong \frac{A_2}{\eta_2 \varepsilon_2 F_2 N_{Na}} \frac{N_{Al}}{N_T} \frac{F_{Na}}{\lambda_{Na}} \sigma_{st} \left(1 - \frac{\lambda_2}{\lambda_1} \right).\end{aligned}\quad (14)$$

In the case where the condition $\sigma_2^{ind} \ll \sigma_1^{cum} \nu_1$ is not satisfied, so the σ_2^{cum} value cannot be calculated in any way accurately, we may estimate the difference

$$\Delta \sigma_2^{cum*} = \sigma_2^{cum*} - \sigma_2^{cum} = \frac{\lambda_2}{\lambda_1 - \lambda_2} \nu_1 \sigma_1^{cum}. \quad (15)$$

Proceeding from the condition $\sigma_2^{cum*} \geq \sigma_2^{cum} \geq \sigma_1^{cum} \nu_1$, we may estimate the upper limit of $\Delta \sigma_2^{cum*}$:

$$\Delta \sigma_2^{cum*} \leq \frac{\lambda_2}{\lambda_1 - \lambda_2} \sigma_2^{cum*} \quad (16)$$

or, in the relative form,

$$\delta \sigma_2^{cum} = \frac{\Delta \sigma_2^{cum*}}{\sigma_2^{cum*}} \cdot 100\% \leq \frac{\lambda_2}{\lambda_1 - \lambda_2} \cdot 100\%. \quad (17)$$

From the resultant formula (16) it is seen that the measured value of the supra cumulative yield σ_2^{cum*} may sometimes prove to be very different from its true value σ_2^{cum} . In the case of ^{179}Re , for example, the data of the present work give a $\delta \sigma_2^{cum}$ value of $\sim 55\%$. This fact should be borne in mind when comparing between experimental and simulated data.

III. EXPERIMENTAL TECHNIQUES

The used experimental techniques are described in [6]. A 10.5 mm diameter, 139.4 mg/cm² monoisotopic ^{208}Pb metal foil sample (97.2% ^{208}Pb , 1.93% ^{207}Pb , 0.87% ^{206}Pb , <0.01% ^{204}Pb , < 0.00105% of chemical impurities) was irradiated by protons. A 139.6 mg/cm² Al foil of the same diameter was used as monitor. Chemical impurities in the monitor do not exceed 0.001%.

The sample was irradiated by the 995 MeV external proton beam of the ITEP U-10 synchrotron described briefly in [6]. The irradiation time was an hour. The total proton fluence was $5 \cdot 10^{13}$ p/cm². The γ -spectrometer measurements began 10 minutes after the irradiation stopped. The spectra have been measured for half a year.

It should be noted that the experimental program of measuring the reaction product yields from diverse materials was supported by other studies aimed at reducing the systematic errors in the experimental results [13]. These studies include:

- experiments to specify the neutron component in the extracted proton beams,
- experiments to specify the monitor-reaction cross section,
- experiments to specify the variations of the γ -spectrometer detection efficiency, depending on the height of the irradiated sample position above the detector,
- studies to optimize the γ -spectrum processing codes.

The results of these studies were used in determining the cross sections for nuclide production in the measured $^{208}\text{Pb}(p,x)$ reactions.

A. Neutron component in the extracted proton beams

The proton beams extracted from accelerators include not only the primary protons, but also secondary particles (neutrons, protons, π mesons, and gammas) produced in the primary proton interactions with the structural materials of transport channels and shielding.

Identical reaction products can be produced in interactions of various secondaries with an experimental sample.

Since particular nuclear reactions that generate a given nuclide cannot be identified in the measurements, the extracted proton beams have to be tested and specified thoroughly.

Track detectors were first used in the experiments to discriminate the neutron component in the proton beams [6]. Later, direct γ spectrometry was used for the purpose. Solid-state nuclear track detectors (SSNTD) of an improved geometry with a collimating grid and a glass fragment track detection material were used to record the fission fragments from a fissile layer, thereby improving the absolute detector efficiency.

An SSNTD with a $61.5 \mu\text{g}/\text{cm}^2$ ^{209}Bi layer was used to measure the proton flux density. ^{209}Bi was selected because the cross section for its fission induced by secondary neutrons is small compared with that for primary protons ($\overline{\sigma}_{^{209}\text{Bi}(n,f)} \ll \sigma_{^{209}\text{Bi}(p,f)}$). The neutron flux density was measured using an SSNTD with a $880 \mu\text{g}/\text{cm}^2$ ^{237}Np layer.

The following experimental design was adopted. The extracted proton beam irradiates a ^{209}Bi -containing “sandwich” (Bi layer + collimator + glass), while similar sandwiches with ^{237}Np layers are placed along a line normal to the beam axis at distances of 20–435 mm from the axis.

In the experiments, the neutron-to-proton flux density ratio, Φ_n/Φ_p , was measured using the expression

$$\frac{\Phi_n}{\Phi_p} = \frac{T_1}{T_2} \cdot \frac{\sigma_{p,f}^{209\text{Bi}}}{\overline{\sigma}_{n,f}^{237\text{Np}}} \cdot \frac{N^{209\text{Bi}}}{N^{237\text{Np}}} \cdot \frac{\xi_2}{\xi_1}, \quad (18)$$

where T_1 and T_2 are numbers of measured tracks of ^{237}Np and ^{209}Bi fission products, respectively; $N^{237\text{Np}}$ and $N^{209\text{Bi}}$ are numbers of the ^{237}Np and ^{209}Bi nuclei, respectively; ξ_1 and ξ_2 are, respectively, corrections to the ^{237}Np and ^{209}Bi layers, which allow for the anisotropy of fission-fragment ejection and for the variations of the solid angle of fission-fragment ejection through the collimator grid; $\sigma_{p,f}^{209\text{Bi}}$ is the cross section for proton-induced ^{209}Bi fission; $\overline{\sigma}_{n,f}^{237\text{Np}}$ is the weighted mean ^{237}Np neutron-induced fission cross section calculated as

$$\overline{\sigma}_x = \frac{\int \sigma_x(E)\Phi(E)dE}{\int \Phi(E)dE}, \quad (19)$$

where

x stands for $^{237}\text{Np}(n,f)$, $^{27}\text{Al}(n,p)^{27}\text{Mg}$, $^{27}\text{Al}(n,x)^{24}\text{Na}$, and $^{27}\text{Al}(n,x)^{22}\text{Na}$.

The fission cross section $\sigma_{n,f}^{237\text{Np}}(E)$ needed to calculate $\overline{\sigma}_{n,f}^{237\text{Np}}$ was retrieved from the WIND data library [14]. The cross section for the proton-induced ^{209}Bi fission, $\sigma_{p,f}^{209\text{Bi}}$, was taken from [15].

The experiments were made with 200, 800, and 2600 MeV proton beams. Fig. 2 shows the resultant Φ_n/Φ_p ratios as functions of the perpendicular distance to the proton beam. The Φ_n/Φ_p ratio right in the proton beam

was estimated by extrapolating the peripheral results to the center and proved to be of about (0.2–2)%.

The feasibility of distinguishing the (n,p) reactions from (p,x) reactions has permitted an alternative pattern of direct γ spectrometry. Namely, Al samples were irradiated, and $^{27}\text{Al}(n,p)^{27}\text{Mg}$ (a ~ 2.5 MeV threshold), $^{27}\text{Al}(n,\alpha)^{24}\text{Na}$ (a ~ 5.5 MeV threshold) + $^{27}\text{Al}(p,x)^{24}\text{Na}$ (a ~ 25 MeV threshold), $^{27}\text{Al}(n,x)^{22}\text{Na}$, and $^{27}\text{Al}(n,x)^7\text{Be}$ reaction rates were measured, in the beam center and at periphery. The $^{27}\text{Al}(n,p)^{27}\text{Mg}$ reaction characteristics have made it possible to detect ^{27}Mg in the experimental ^{27}Al samples positioned normally to the proton beam axis at the beam center and at distances of 40–430 mm from the beam axis. The $^{27}\text{Al}(n,p)^{27}\text{Mg}$ cross sections were derived from the MENDL2 library [16]. The distance-dependent Φ_n/Φ_p ratios measured via $^{27}\text{Al}(n,p)^{27}\text{Mg}$ reaction are shown in Fig. 2 together with the results of the SSNTD method.

The technique has also made it possible to detect ^{27}Mg together with ^{24}Na , ^{22}Na , and ^7Be , when ^{27}Al was irradiated in the proton beam. In this case, the neutron-to-proton flux density ratio in the beam is estimated as

$$\frac{\Phi_n}{\Phi_p} = \frac{\frac{\sigma_{p,x}^{7\text{Be}, 22\text{Na}, 24\text{Na}}}{\overline{\sigma}_{n,p}^{27\text{Mg}}}}{\frac{N^{7\text{Be}, 22\text{Na}, 24\text{Na}}}{N^{27\text{Mg}}} - \frac{\overline{\sigma}_{n,x}^{7\text{Be}, 22\text{Na}, 24\text{Na}}}{\overline{\sigma}_{n,p}^{27\text{Mg}}}}, \quad (20)$$

where $\overline{\sigma}_{n,p}^{27\text{Mg}}$, $\overline{\sigma}_{n,x}^{22\text{Na}}$, $\overline{\sigma}_{n,x}^{7\text{Be}}$, and $\overline{\sigma}_{n,x}^{24\text{Na}}$ are the neutron spectrum-weighted cross sections of the above reactions calculated by formula (19) using the excitation functions from MENDL2 database [16]; $\sigma_{p,x}^{22\text{Na}}$, $\sigma_{p,x}^{24\text{Na}}$, and $\sigma_{p,x}^{7\text{Be}}$ are the $^{27}\text{Al}(p,x)^{24}\text{Na}$, $^{27}\text{Al}(p,x)^{22}\text{Na}$, and $^{27}\text{Al}(p,x)^7\text{Be}$ reaction cross sections; $N^{24\text{Na}}$, $N^{22\text{Na}}$, $N^{27\text{Mg}}$, and $N^{7\text{Be}}$ are numbers of the ^{24}Na , ^{22}Na , ^{27}Mg , and ^7Be nuclei produced in the Al samples with allowance for their decays under irradiation.

The techniques described above were used in the experiments with proton beams of 0.07, 0.1, 0.13, 0.2, 0.8, 1.0, 1.6, and 2.6 GeV.

As seen from Figs. 2 and 3, the neutron component estimates obtained by the both techniques (SSNTD and γ spectrometry) are essentially the same and are small. It should be noted that the $^{208}\text{Pb}(p,x)$ reaction products measured at 1 GeV proton energy (see Table II) include none of the nuclides producible in the (n,xn) reactions up to $x = 5$ (^{204m}Pb), for such nuclides are either stable or long-lived. Our estimates have shown that, in the case of Pb isotopes of masses less than or equal to ^{204}Pb , additional production of daughter nuclei by (n,xn) reactions is below the level of experimental errors.

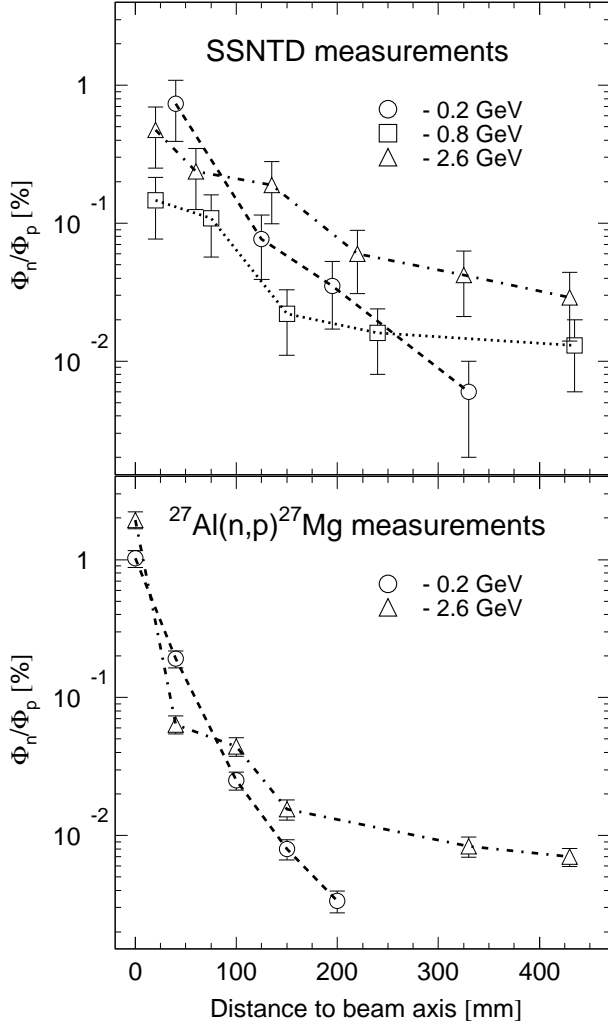


FIG. 2. The neutron-to-proton mean flux density ratios versus distance from the proton beam axis calculated using: (1) the SSNTD measurements (upper plot); (2) $^{27}\text{Al}(n,p)^{27}\text{Mg}$ measurements (bottom plot).

B. Monitor reactions

Contrary to [6], the present work uses the $^{27}\text{Al}(p,x)^{22}\text{Na}$ monitor reaction. Current practice suggests that three monitor reactions should be used on ^{27}Al , namely, $^{27}\text{Al}(p,x)^{24}\text{Na}$ for short-term irradiations, $^{27}\text{Al}(p,x)^{22}\text{Na}$ and $^{27}\text{Al}(p,x)^7\text{Be}$ for long-term irradiations.

Therefore, we have made additional experiments to study the ^{24}Na and ^7Be yields relative to ^{22}Na . The ^{22}Na cross section values were obtained from [17]. Since ^{24}Na , ^7Be , and ^{22}Na are produced in one and the same irradiated sample, their cross section ratios (represented by $\sigma^{24\text{Na}}/\sigma^{22\text{Na}}$, as an example) in a general form allowing for the neutron component can be calculated as

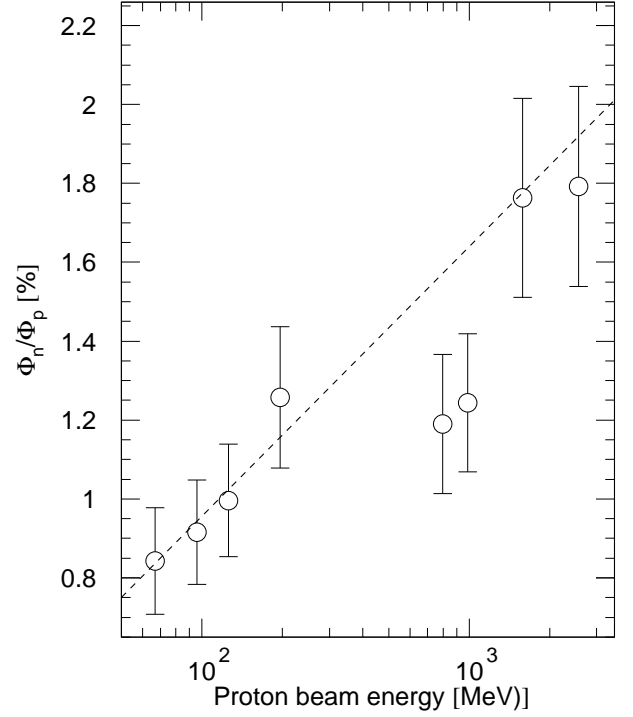


FIG. 3. The neutron-to-proton mean flux density ratios in the proton beam versus proton energy as calculated from the γ -spectrometry data.

$$\frac{\sigma^{24\text{Na},7\text{Be}}}{\sigma^{22\text{Na}}} = \frac{A_0^{24\text{Na},7\text{Be}}}{A_0^{22\text{Na}}} \frac{(\eta\varepsilon)^{22\text{Na}}}{(\eta\varepsilon)^{24\text{Na},7\text{Be}}} \frac{F^{22\text{Na}}}{F^{24\text{Na},7\text{Be}}} \times \frac{1 + \left(\frac{\bar{\sigma}_{n,x}^{22\text{Na}} \Phi_n}{\sigma_{p,x}^{22\text{Na}} \Phi_p} \right)}{1 + \left(\frac{\bar{\sigma}_{n,x}^{24\text{Na},7\text{Be}} \Phi_n}{\sigma_{p,x}^{24\text{Na},7\text{Be}} \Phi_p} \right)}. \quad (21)$$

Since the Φ_n/Φ_p ratio does not exceed $\sim 2\%$ at any proton beam energy (see Fig. 3), the following simplified formula can be used:

$$\frac{\sigma^{24\text{Na},7\text{Be}}}{\sigma^{22\text{Na}}} = \frac{A_0^{24\text{Na},7\text{Be}}}{A_0^{22\text{Na}}} \frac{(\eta\varepsilon)^{22\text{Na}}}{(\eta\varepsilon)^{24\text{Na},7\text{Be}}} \frac{F^{22\text{Na}}}{F^{24\text{Na},7\text{Be}}}. \quad (22)$$

The urgent necessity for high-precision monitoring has made us to extend our measurements to the entire energy range used in our experiments, although a single energy (1 GeV) is treated in the present work. Table I and Fig. 4 show the measurement results.

C. γ -spectrometer detection efficiency allowing for the height factors

The γ spectra have to be measured for a broad range of heights H (the source-detector distances) so that early counting may begin without overwhelmingly large

TABLE I. The monitor reaction cross sections [mb] averaged over the experiments

Proton energy, GeV	The $^{27}\text{Al}(p,x)^{22}\text{Na}$ monitor cross sections used in this work	The measured reaction cross sections. Shown in brackets are the errors disregarding/allowing for the $^{27}\text{Al}(p,x)^{22}\text{Na}$ reaction cross section error	
		$^{27}\text{Al}(p,x)^{24}\text{Na}$	$^{27}\text{Al}(p,x)^7\text{Be}$
0.067	24.4 ± 1.4	$11.3 \pm (0.5 / 0.8)$	$0.76 \pm (0.20 / 0.21)$
0.097	19.1 ± 1.3	$11.0 \pm (0.3 / 0.8)$	$0.97 \pm (0.07 / 0.10)$
0.127	17.0 ± 1.3	$10.1 \pm (0.3 / 0.8)$	$1.14 \pm (0.06 / 0.11)$
0.147	16.1 ± 1.2	$9.7 \pm (0.4 / 0.8)$	$1.44 \pm (0.11 / 0.16)$
0.197	15.1 ± 0.9	$9.8 \pm (0.4 / 0.7)$	$1.48 \pm (0.04 / 0.10)$
0.8	15.5 ± 0.9	$12.7 \pm (0.3 / 0.8)$	$6.3 \pm (0.3 / 0.4)$
1.0	15.0 ± 0.9	$12.5 \pm (0.8 / 1.1)$	$7.5 \pm (0.3 / 0.5)$
1.2	14.6 ± 1.0	$12.8 \pm (0.3 / 0.9)$	$8.3 \pm (0.2 / 0.6)$
1.4	13.9 ± 1.0	$12.7 \pm (0.4 / 1.0)$	$8.9 \pm (0.3 / 0.7)$
1.5	13.5 ± 1.0	$12.8 \pm (0.3 / 1.0)$	$8.8 \pm (0.3 / 0.7)$
1.6	13.2 ± 1.0	$11.6 \pm (0.3 / 0.9)$	$8.9 \pm (0.2 / 0.7)$
2.6	11.7 ± 0.9	$10.6 \pm (0.3 / 0.9)$	$9.2 \pm (0.2 / 0.7)$

counting rates, and later measurements do not suffer from too low rates.

Therefore, the γ spectrometer was efficiency calibrated in a $60 < E_\gamma < 2600$ keV range for nine heights within a 40–550 mm interval using the standard set of γ -radiation sources (^{54}Mn , ^{57}Co , ^{60}Co , ^{88}Y , ^{109}Cd , ^{113}Sn , ^{133}Ba , ^{137}Cs , ^{139}Ce , ^{152}Eu , ^{228}Th , ^{241}Am , and ^{22}Na). The energy dependence of the detection efficiency obtained for a base height was approximated by the cubic spline

$$\varepsilon_{base}(E) = \exp \left[\sum_{i=k}^{k+3} P_i \cdot (\ln E)^{i-k} \right], \quad (23)$$

$$\Delta \varepsilon_{base} = \varepsilon_{base}(E) \times \sqrt{\sum_{i=k}^{k+3} \sum_{j=k}^{k+3} M_{ij}^{-1} (\ln E)^{i+j-2k} \cdot \frac{\chi_\varepsilon^2}{L}}, \quad (24)$$

where

$$k = \begin{cases} 1, & \text{for } \ln E < \ln E_0, \\ 5, & \text{for } \ln E \geq \ln E_0, \end{cases} \quad E_0 = 300 \text{ keV},$$

$$\chi_\varepsilon^2 = \sum_{i=1}^{J_1+J_2} \left[\frac{\varepsilon_{base}^{exp}(E_i) - \varepsilon_{base}(E_i)}{\Delta \varepsilon_{base}^{exp}(E_i)} \right]^2, \quad (25)$$

where $\varepsilon_{base}(E_i)$ and $\Delta \varepsilon_{base}^{exp}(E_i)$ are the value and its absolute error for the calculated efficiency of the spectrometer at the i -th energy E_i ; P_i are polynomial coefficients; M_{ij}^{-1} is the covariance matrix of the polynomial coefficients; L is the number of degrees of freedom when determining χ^2 ; $J_1 + J_2$ is the total number of experimental points; $\varepsilon_{base}^{exp}(E_i)$ and $\Delta \varepsilon_{base}^{exp}(E_i)$ are the experimental values and their absolute errors for the

experimental efficiency of the spectrometer at the i -th energy E_i .

The radioactive reaction products of as long a half-life as possible were sought for and identified for each of the irradiated samples. Therefore, starting from a certain moment, the measurements were made at the lowest height ($H=40$ mm), where the effect of the cascade summation of γ quanta is negligible. The magnitude of this effect was determined experimentally.

An optimal schedule for changing the heights to preserve an approximate constancy of the maximum possible spectrometer load was very difficult to select beginning from the very start moment of measuring a sample irradiated. Therefore, the height dependence of the detection efficiency was analyzed for each of the γ energies of the calibration sources. The analysis has given the dependence expressed as

$$\varepsilon(E, H) = \varepsilon_{base}(E) \cdot \left[\frac{(q_1 + q_2 \cdot \ln E + H_{base})}{(q_1 + q_2 \cdot \ln E + H)} \right]^2, \quad (26)$$

$$\Delta \varepsilon(E, H) = \varepsilon(E, H) \sqrt{\left[\frac{\Delta \varepsilon_{base}}{\varepsilon_{base}} \right]^2 + 4(H - H_{base})^2 \times \frac{(V_{11}^{-1} + 2V_{12}^{-1} \cdot \ln E + V_{22}^{-1} \cdot (\ln E)^2) \cdot \chi_q^2}{[q_1 + q_2 \cdot \ln E + H_{base}]^2 \cdot [q_1 + q_2 \cdot \ln E + H]^2}}, \quad (27)$$

where $\varepsilon(E, H)$ and $\Delta \varepsilon(E, H)$ are, respectively, the value and the absolute error for the dependence of the spectrometer detection efficiency on energy and height; q_1 and q_2 are the fitting parameters; V_{ij}^{-1} are the covariance matrix elements of the parameters q_1 and q_2 ; χ_q^2 is given by Eq. (25).

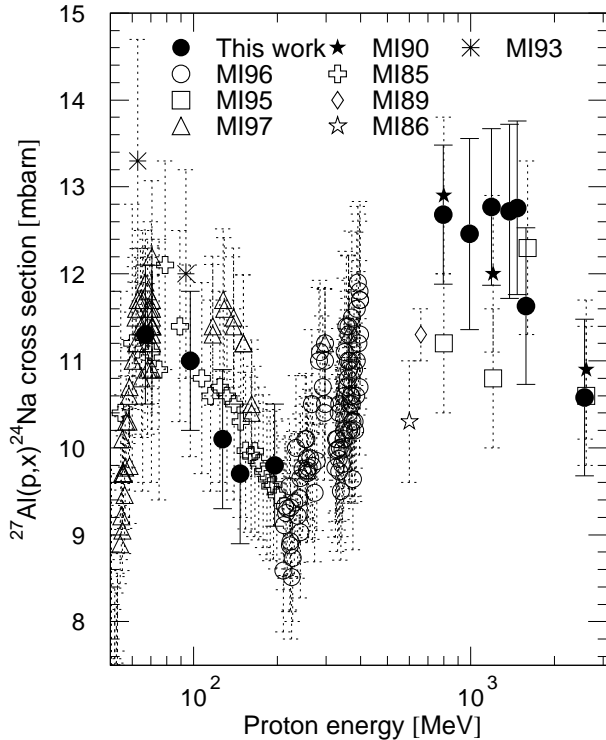


FIG. 4. The $^{27}\text{Al}(p,x)^{24}\text{Na}$ monitor cross sections measured in this work and from previous works: MI85 – [18], MI86 – [19], MI89 – [20], MI90 – [21], MI93 – [22], MI95 – [7], MI96 – [23], MI97 – [24].

From formula (26) it is readily seen that any of the above mentioned heights can be selected, but the extreme heights are not desirable, for they involve a rise of the systematic error when renormalizing the rest of the heights to the basic height. If, however, the height of the prevailing measurements is selected, the systematic error decreases during the renormalization.

Fig. 5 shows the detection efficiencies measured at different heights (the dots). The curves in the figure present the dependence of the efficiencies on height and energy as inferred from formula (26).

The analysis based on formulas (24) and (27) has shown that the systematic errors due to uncertainties in the detection efficiency do not exceed 5%.

D. Processing of γ spectra and cross section determination

The measured γ spectra of irradiated ^{208}Pb are extremely complicated due to the numerous γ lines. Despite using the Ge detector with its ultimate attained resolution, the spectra still include many multiplets, so the GENIE-2000 code [25] which is designed to process complicated γ spectra has been used. The code is notable

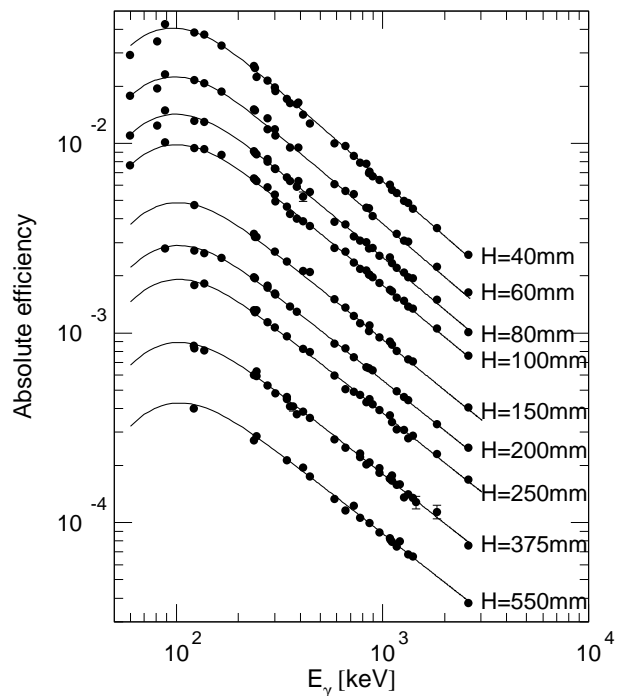


FIG. 5. The measured and simulated height-energy detection efficiency of the CANBERRA GC2518 Ge-detector-based γ spectrometer for different heights of the γ source.

for permitting the results of tentative processing to be analyzed again after the computer-aided consolidated processing of the γ spectra by interactive fitting of the γ peaks. Namely, we find out whether the peak regions are either multiplets, real peaks that fail to satisfy the search criteria, spurious peaks, etc.

The interactive processing has made it possible to improve the accuracy and reliability of analysis of the measured γ spectra, especially in the case of poorly resolved spectra with poor statistics.

The processed γ spectra are then united to form the input file for the ITEP-developed SIGMA code, which plots the time variations of a selected γ -line intensity and makes use of the energy and the half-life of that γ line to identify the product nuclide using the PCNUDAT database [26] and the Firestone's Table of Isotopes [27] and to determine the product nuclide cross sections using formulas (1)–(4).

IV. MEASURED PRODUCT YIELDS FROM THE $^{208}\text{Pb}(P,X)$ REACTION

Table II presents the results of determining the reaction product yields in 1 GeV proton-irradiated ^{208}Pb . Out of 114 yields presented, 8 are independent yields of ground states(i), 15 are independent yields of metastable states ($i(\Sigma m_j)$), 15 are independent yields of metastable and ground states ($i(\Sigma m_j+g)$), 65 are cumulative yields (c), and 11 are supra cumulative yields, when the

correction may exceed the determination error (c^*). It should be noted that in case the (c) values are to be reconstructed from (c^*) using of formula (15), we must have the σ_1^{cum} values that have yet to be determined, but are expected to be measured in the future. As mentioned above, however, the simulation codes can be tested using the (c^*) values.

From Table II we see that the experimental errors range from 7% to 30%. The tabulated values are calculated as follows. Since most of the results are obtained by averaging over a set of ($\sigma_i \pm \Delta\sigma_i$) values calculated from different γ lines, the mean and the experimental errors were calculated as

$$\bar{\sigma} = \frac{\sum_i \sigma_i W_i}{\sum_i W_i}, \quad \text{where} \quad W_i = 1/\Delta\sigma_i^2. \quad (28)$$

The $\Delta\sigma_i$ were determined using the error propagation formulas [28]

$$\Delta\bar{\sigma}' = \sqrt{\frac{\sum_i W_i (\bar{\sigma} - \sigma_i)^2}{(n-1) \sum_i W_i}}, \quad (29)$$

$$\Delta\bar{\sigma}'' = \sqrt{\frac{1}{\sum_i W_i}}. \quad (30)$$

In the calculations, the largest of $\Delta\bar{\sigma}'$ and $\Delta\bar{\sigma}''$ was taken to be the experimental error $\Delta\bar{\sigma}$. Allowing for the monitor error, the total error in the measured cross sections was calculated as

$$\frac{\Delta\bar{\sigma}}{\bar{\sigma}} = \sqrt{\left(\frac{\Delta\bar{\sigma}}{\bar{\sigma}}\right)^2 + \left(\frac{\Delta\sigma_{st}}{\sigma_{st}}\right)^2}. \quad (31)$$

Our analysis has shown that the main contribution to the total error is from uncertainties in the nuclear data (the absolute gamma yields and cross sections of the monitor reactions).

V. COMPARISON WITH EXPERIMENTAL DATA OBTAINED ELSEWHERE

In addition to the nuclide production cross sections measured in this work, Table II also presents data from other works, namely, the results obtained by the ‘‘inverse kinematics’’ technique (^{208}Pb bombarding ^1H at GSI [8]) and the results of measuring the nuclide production in 1 GeV proton-irradiated ^{nat}Pb obtained by a technique that is similar to ours by the group of R. Michel at Hannover University, Zentrum für Strahlenschutz und Radioökologie (ZSR) [29].

It should be noted that the GSI data are measured only as independent yields, so they are summed up for their isobaric chains to be compared with the respective cumulative yields determined at ITEP and ZSR. We estimated

errors for the GSI cumulative yields as square roots of sums of squared errors of all independent yields contributing to the corresponding cumulative cross sections and also took into account their systematic errors which vary from 9 to 25% [8]. The GSI technique does not distinguish if a product nuclide is in a ground or metastable state, hence, we do not compare our data with the GSI set in the case we measured only metastable or ground states (^{204m}Pb , ^{197m}Pb , $^{198m1}\text{Tl}$, ^{196m}Tl , ^{197m}Hg , ^{195m}Hg , ^{193m}Hg , ^{198m}Au , ^{198g}Au , ^{186g}Ir , ^{183m}Os , ^{182m}Re , ^{121m}Te , ^{119m}Te , ^{120m}Sb , ^{114m}In , ^{110m}Ag , ^{106m}Ag , ^{101m}Rh , ^{90m}Y , and ^{82m}Rb) as well as when there is a transition of a metastable state to a product out of the given decay chain (^{198}Tl , ^{190}Ir , ^{152}Tb , ^{149}Gd , ^{121}Te , ^{96}Tc , ^{95}Tc , ^{95}Nb , ^{95}Nb , ^{89}Zr , ^{87}Y , and ^{85}Sr).

Let us mention here that the ZSR work [29] was carried out using natural lead, rather than high ^{208}Pb -enriched lead used at ITEP and GSI. We think, it is this fact that can be primarily responsible for some divergences between the ZSR data and the GSI and ITEP ones. The importance of this circumstance is indirectly confirmed by a 1.5 times higher mean-squared deviation of the ZSR data from the GSI data compared with the mean-squared deviation of the ITEP data from the same GSI data. The mean-squared deviations between two data sets (1 and 2) calculated as $\langle F_{1-2} \rangle = 100\% \times (10^{\sqrt{D}} - 1)$ (where $D = \langle \log(\sigma_{1i}/\sigma_{2i})^2 \rangle$) proved to be 48% and 32% for ZSR–GSI and ITEP–GSI comparisons, respectively.

VI. SIMULATION OF EXPERIMENTAL DATA

The present work is aimed at determining the nuclear cross sections to be used in designing ADS facilities. An attempt to obtain the necessary nuclear cross sections only from experiments would involve impractical levels of expense and effort. Therefore, simulation techniques must be used for that purpose. The simulation approach has the advantage that it also can be used for many other purposes. On the other hand, the current accuracy and reliability of simulated data are inferior to experiment. Also existing simulation codes have different predictive abilities when used to study the reactions that are of practical importance.

Considering this, the present work is aimed also at verifying the simulation codes used most extensively for this purpose in order to estimate their predictive abilities and to stimulate efforts to improve them.

The following seven simulation codes were examined to meet these requirements:

- the CEM95 cascade-exciton model code [30],
- the latest version of the improved cascade-exciton model [31] code, CEM2k, [32],
- the CASCADE cascade-evaporation-fission transport code [33],

TABLE II. Experimental product nuclide yields [mb] in 1 GeV proton-irradiated ^{208}Pb compared with both recent GSI data measured in inverse kinematics [8] and the ZSR measurements on ^{nat}Pb [29]

Product	$T_{1/2}$ [26], [27]	Type	Yield (this work)	Work [8]	Work [29]
^{206}Bi	6.243d	i	4.60 ± 0.29	–	5.36 ± 0.67
^{205}Bi	15.31d	i	6.20 ± 0.40	–	7.09 ± 0.90
^{204}Bi	11.22h	i(m1+m2+g)	5.29 ± 0.80	–	6.03 ± 0.95
^{203}Bi	11.76h	i(m+g)	4.84 ± 0.59	–	–
^{204m}Pb	67.2m	i(m)	11.0 ± 1.0	–	–
^{203}Pb	51.873h	c	31.5 ± 2.1	28.7 ± 3.1	–
^{201}Pb	9.33h	c*	26.9 ± 2.4	20.4 ± 1.9	–
^{200}Pb	21.5h	c	18.2 ± 1.2	18.2 ± 2.0	27.8 ± 3.5
^{198}Pb	2.4h	c	8.9 ± 2.1	14.0 ± 1.3	–
^{197m}Pb	43m	c*	17.9 ± 4.0	–	–
^{202}Tl	12.23d	c	18.8 ± 1.2	40.0 ± 4.0	22.0 ± 2.7
^{201}Tl	72.912h	c	43.7 ± 2.9	37.3 ± 3.7	53.5 ± 6.6
^{200}Tl	26.1h	c	40.6 ± 2.6	35.2 ± 3.7	–
^{200}Tl	26.1h	i(m+g)	22.7 ± 1.5	17.0 ± 1.7	22.3 ± 6.1
^{199}Tl	7.42h	c	38.5 ± 5.2	34.3 ± 3.4	–
$^{198m1}\text{Tl}$	1.87h	i(m1+m2)	17.6 ± 3.6	–	–
^{198}Tl	5.3h	c	35.9 ± 5.0	–	–
^{196m}Tl	1.41h	i(m)	34.8 ± 4.4	–	–
^{203}Hg	46.612d	c	4.03 ± 0.27	–	3.66 ± 0.45
^{197m}Hg	23.8h	i(m)	10.7 ± 0.7	–	–
^{195m}Hg	41.6h	i(m)	13.6 ± 2.0	–	13.3 ± 1.8
^{193m}Hg	11.8h	i(m)	18.9 ± 2.5	–	10.8 ± 2.3
^{192}Hg	4.85h	c	35.2 ± 2.8	31.3 ± 3.4	–
^{198m}Au	2.27d	i(m)	1.01 ± 0.14	–	1.25 ± 1.11
^{198}Au	2.69517d	i(m+g)	2.11 ± 0.22	1.96 ± 0.23	–
^{198}Au	2.69517d	i	1.09 ± 0.30	–	–
^{196}Au	6.183d	i(m1+m2+g)	4.13 ± 0.35	4.02 ± 0.47	3.88 ± 0.47
^{195}Au	186.098d	c	48.7 ± 5.5	28.4 ± 3.3	51.1 ± 6.6
^{194}Au	38.02h	i(m1+m2+g)	7.06 ± 0.75	6.33 ± 0.75	6.85 ± 0.92
^{192}Au	4.94h	c	46.9 ± 6.6	39.9 ± 4.6	–
^{192}Au	4.94h	i(m1+m2+g)	11.6 ± 1.7	9.2 ± 1.1	–
^{191}Pt	2.802d	c	41.8 ± 4.2	44.4 ± 5.5	37.9 ± 4.8
^{189}Pt	10.87h	c	46.8 ± 4.8	40.4 ± 5.0	–
^{188}Pt	10.2d	c	40.5 ± 2.9	38.4 ± 4.7	42.8 ± 5.4
^{186}Pt	2.08h	c*	33.5 ± 2.3	32.9 ± 4.1	–
^{190}Ir	11.78d	i(m1+g)	0.69 ± 0.06	–	–
^{188}Ir	41.5h	c	43.2 ± 3.2	40.9 ± 5.4	–
^{188}Ir	41.5h	i	2.93 ± 0.69	2.48 ± 0.33	–
^{186}Ir	16.64h	i	20.8 ± 1.9	–	22.5 ± 3.1
^{185}Ir	14.4h	c*	34.8 ± 2.3	39.4 ± 5.2	39.4 ± 7.9
^{184}Ir	3.09h	c*	39.5 ± 3.0	36.9 ± 4.8	–
^{185}Os	93.6d	c	41.8 ± 2.8	38.1 ± 5.3	43.0 ± 5.3
^{183m}Os	9.9h	c	23.2 ± 1.5	–	–
^{182}Os	22.10h	c	42.0 ± 2.8	34.2 ± 4.8	–
^{183}Re	70.0d	c	41.7 ± 2.9	36.3 ± 5.3	38.2 ± 4.8
^{182m}Re	12.7h	c	45.2 ± 3.7	–	–
^{181}Re	19.9h	c	43.1 ± 5.9	37.0 ± 5.4	45.9 ± 5.9
^{179}Re	19.5m	c*	48.2 ± 4.2	44.7 ± 6.6	–
^{177}W	135m	c	30.1 ± 3.5	23.4 ± 3.6	–
^{176}W	2.5h	c	28.0 ± 3.9	29.0 ± 4.5	–
^{176}Ta	8.09h	c	35.0 ± 3.6	28.8 ± 4.7	–
^{173}Ta	3.14h	c	30.9 ± 3.9	26.3 ± 4.3	–
^{172}Ta	36.8m	c*	17.3 ± 2.3	27.4 ± 4.5	–
^{175}Hf	70d	c	31.3 ± 2.3	28.3 ± 4.8	34.1 ± 4.1
^{173}Hf	23.6h	c	28.4 ± 2.6	25.2 ± 4.3	39.0 ± 4.9
^{172}Hf	1.87y	c	24.1 ± 1.6	24.6 ± 4.2	24.4 ± 3.1

Product	$T_{1/2}$	Type	Yield (this work)	Work [8]	Work [29]
¹⁷¹ Hf	12.1h	c	18.2 ± 2.8	22.9 ± 3.9	–
¹⁷⁰ Hf	16.01h	c	22.1 ± 6.8	20.3 ± 3.5	21.2 ± 3.0
¹⁷² Lu	6.70d	c	23.9 ± 1.7	24.7 ± 4.4	–
¹⁷² Lu	6.70d	i(m1+m2+g)	0.19 ± 0.05	0.183 ± 0.037	–
¹⁷¹ Lu	8.24d	c	26.1 ± 1.8	16.6 ± 3.0	31.3 ± 3.9
¹⁷⁰ Lu	2.012d	c	21.7 ± 2.9	20.9 ± 3.7	–
¹⁶⁹ Lu	34.06h	c	18.6 ± 1.2	12.1 ± 2.2	26.4 ± 3.7
¹⁶⁹ Yb	32.026d	c	20.9 ± 1.5	18.1 ± 3.4	24.3 ± 3.0
¹⁶⁶ Yb	56.7h	c	16.1 ± 1.1	13.7 ± 2.6	16.4 ± 2.3
¹⁶⁷ Tm	9.25d	c	19.4 ± 4.0	14.0 ± 2.7	21.2 ± 2.6
¹⁶⁵ Tm	30.06h	c	14.4 ± 1.4	13.3 ± 2.6	–
¹⁶⁰ Er	28.58h	c	8.8 ± 0.6	7.2 ± 1.5	–
¹⁵⁷ Dy	8.14h	c	5.73 ± 0.45	5.0 ± 1.1	–
¹⁵⁵ Dy	9.9h	c*	3.66 ± 0.27	2.86 ± 0.63	–
¹⁵⁵ Tb	5.32d	c	4.16 ± 0.39	2.72 ± 0.62	5.52 ± 0.70
¹⁵³ Tb	2.34d	c*	2.52 ± 0.25	2.40 ± 0.54	2.51 ± 0.40
¹⁵² Tb	17.5h	c*	2.10 ± 0.17	–	–
¹⁵³ Gd	240.4d	c	2.65 ± 0.24	2.18 ± 0.51	3.10 ± 0.38
¹⁴⁹ Gd	9.28d	c	2.24 ± 0.18	–	3.06 ± 0.38
¹⁴⁶ Gd	48.27d	c	1.26 ± 0.09	1.23 ± 0.29	1.68 ± 0.21
¹⁴⁷ Eu	24.1d	c	0.98 ± 0.30	1.18 ± 0.29	1.97 ± 0.29
¹⁴⁶ Eu	4.61d	c	1.62 ± 0.12	1.17 ± 0.28	–
¹⁴⁶ Eu	4.61d	i	0.37 ± 0.05	0.181 ± 0.047	–
¹⁴³ Pm	265d	c	1.02 ± 0.13	0.85 ± 0.22	1.00 ± 0.13
¹³⁹ Ce	137.640d	c	0.83 ± 0.06	0.45 ± 0.13	0.82 ± 0.10
^{121m} Te	154d	i(m)	0.44 ± 0.04	–	0.53 ± 0.07
¹²¹ Te	19.16d	c	1.07 ± 0.11	–	0.79 ± 0.10
^{119m} Te	4.70d	i(m)	0.40 ± 0.04	–	–
^{120m} Sb	5.76d	i(m)	0.54 ± 0.05	–	0.53 ± 0.07
^{114m} In	49.51d	i(m1+m2)	0.95 ± 0.19	–	1.07 ± 0.16
^{110m} Ag	249.76d	i(m)	1.11 ± 0.09	–	1.32 ± 0.17
^{106m} Ag	8.28d	i(m)	0.89 ± 0.08	–	0.92 ± 0.14
¹⁰⁵ Ag	41.29d	c	0.65 ± 0.12	0.74 ± 0.17	1.04 ± 0.14
¹⁰⁵ Rh	35.36h	c	4.63 ± 0.54	3.13 ± 0.51	–
^{101m} Rh	4.34d	c	1.29 ± 0.16	–	–
¹⁰³ Ru	39.26d	c	3.84 ± 0.26	3.03 ± 0.50	4.11 ± 0.53
⁹⁶ Tc	4.28d	i(m+g)	1.20 ± 0.09	–	1.49 ± 0.19
⁹⁵ Tc	20.0h	c	1.38 ± 0.13	–	–
⁹⁶ Nb	23.35h	i	2.31 ± 0.19	2.13 ± 0.34	–
⁹⁵ Nb	34.975d	c	5.41 ± 0.34	–	–
⁹⁵ Nb	34.975d	i(m+g)	3.03 ± 0.20	–	3.58 ± 0.56
⁹⁵ Zr	64.02d	c	2.34 ± 0.15	1.58 ± 0.28	2.32 ± 0.29
⁸⁹ Zr	78.41h	c	2.30 ± 0.16	–	2.82 ± 0.35
⁸⁸ Zr	83.4d	c	0.76 ± 0.08	0.97 ± 0.15	1.19 ± 0.15
^{90m} Y	3.19h	i(m)	4.82 ± 0.39	–	–
⁸⁸ Y	106.65d	c	4.03 ± 0.27	3.72 ± 0.58	–
⁸⁸ Y	106.65d	i(m+g)	3.41 ± 0.25	2.76 ± 0.44	3.74 ± 0.46
⁸⁷ Y	79.8h	c*	2.94 ± 0.23	–	3.36 ± 0.42
⁸⁵ Sr	64.84d	c	2.76 ± 0.22	–	3.42 ± 0.41
⁸⁶ Rb	18.631d	i(m+g)	5.48 ± 0.66	2.43 ± 0.38	4.39 ± 0.61
⁸³ Rb	86.2d	c	3.46 ± 0.28	2.82 ± 0.45	3.96 ± 0.49
^{82m} Rb	6.472h	i(m)	2.73 ± 0.30	–	–
⁸² Br	35.30h	i(m+g)	2.17 ± 0.14	1.55 ± 0.24	2.62 ± 0.50
⁷⁵ Se	119.779d	c	1.33 ± 0.09	1.18 ± 0.19	1.61 ± 0.20
⁷⁴ As	17.77d	i	1.86 ± 0.18	1.66 ± 0.27	2.24 ± 0.28
⁵⁹ Fe	44.472d	c	0.91 ± 0.08	0.69 ± 0.11	1.05 ± 0.14
⁶⁵ Zn	244.26d	c	0.79 ± 0.19	0.42 ± 0.07	0.66 ± 0.17
⁴⁶ Sc	83.79d	i(m+g)	0.35 ± 0.06	–	0.37 ± 0.05

- the INUCL cascade-preequilibrium-evaporation-fission code [34],
- the LAHET (both ISABEL and Bertini options) cascade-preequilibrium-evaporation-fission transport code [35],
- the YIELDX semi-phenomenological code [36],
- the CASCADE/INPE cascade-evaporation-preequilibrium-fission-transport code [37].

All the codes, except for CASCADE/INPE and CEM2k are described in some detail in [6].

The intranuclear part of the CASCADE/INPE code package [37], based on the Dubna cascade model [38], is used to simulate the characteristics of projectile interactions with target nuclei. Recently the code was upgraded at the Institute of Nuclear Power Engineering (Obninsk, Russia) [37]. Principal modifications of the code include:

- a special routine for calculating the precompound spectra of α particles, which have been demonstrated to play an important role in the production of long-lived radioactivity in different heavy targets;
- the code was upgraded to allow for the description of angular distributions of nucleons based on the Kalbach parametrization for projectile energies below 0.8 GeV;
- a new realization of the Weisskopf evaporation approach used in [38] has been introduced. This is based on inverse-reaction cross-section calculations using various optical potentials appropriate for various mass and energy regions; nuclear level densities are calculated taking into consideration nucleon pairing to evaluate the excitation energy of residual nuclei;
- the latest version of the mass table of the nuclides [39] has been used for binding-energy calculations.

The improved Cascade-Exciton Model (CEM) of nuclear reactions [31] was developed and incorporated in the code CEM97 in the Theoretical Division of Los Alamos National Laboratory, as an improvement to the code CEM95 [30]. It is described in detail in [31], therefore we will not elaborate here. CEM2k is a next step in the improvement of the CEM; it differs from CEM97 mainly in the details of the transitions from the cascade stage of a reaction to the preequilibrium one, and from the latter to equilibrium decay. This preliminary version of CEM2k has less preequilibrium emission than the earlier versions. The changes were motivated by discrepancies with the recent GSI data [8] in the earlier versions of the model. It is briefly surveyed in [32], it is still under development and will be described in a future paper.

Contrary to the simulated data, the experimental results include not only independent, but also (and

mainly) cumulative and supra cumulative, residual product nuclei. To get a correct comparison between the experimental and simulation data, the cumulative yields must be calculated on the basis of the simulated independent yields. If the production chain of n radioactive nuclei is presented as

$$\begin{array}{ccccccc} \sigma_1 & & \sigma_2 & & \dots & & \sigma_n \\ \downarrow & & \downarrow & & & & \downarrow \\ 1 & \xrightarrow{\nu_1} & 2 & \xrightarrow{\nu_2} & \dots & \xrightarrow{\nu_{n-1}} & n \end{array} \quad (33)$$

(where ν_1, \dots, ν_{n-1} are the branching ratios of the respective nuclides), the simulated cumulative and supra cumulative yields of the n -th nuclide can be calculated as

$$\sigma_n^{cum} = \sigma_n^{ind} + \sum_{i=1}^{n-1} \left(\sigma_i^{ind} \prod_{j=i}^{n-1} \nu_j \right), \quad (33)$$

$$\begin{aligned} \sigma_n^{cum*} &= \sigma_n^{ind} + \frac{\lambda_{n-1}}{\lambda_{n-1} - \lambda_n} \nu_{n-1} \\ &\times \left[\sigma_{n-1}^{ind} + \sum_{i=1}^{n-2} \left(\sigma_i^{ind} \prod_{j=i}^{n-2} \nu_j \right) \right]. \end{aligned} \quad (34)$$

The branching ratios of the decay chains were taken from [27], considering that the branched (due to isomeric transitions and α decay) isobaric chains can always be presented as a superposition of linear chains.

To get a correct comparison between results obtained by different codes, the calculations were renormalized to the same cross sections for proton-nucleus inelastic interactions. We calculated these cross sections by the semi-empirical formula [40]

$$\begin{aligned} \sigma_{inel} &= 45A^{0.7} f(A)g(E), \quad (\text{in mb}) \\ f(A) &= 1 + 0.016 \sin(5.3 - 2.63 \log A), \\ g(E) &= 1 - 0.62 \exp(-E/200) \sin(10.9E - 0.28), \end{aligned} \quad (35)$$

where A is the mass number of the target and E is the energy (in MeV) of the projectile proton.

The cross section for the $p+^{208}\text{Pb}$ inelastic interactions as calculated by formula (35) is of 1857.8 mb at 995 MeV, the incident energy of our experiment.

If an experiment-simulation difference of no more than 30% ($0.77 < \sigma_{calc}/\sigma_{exp} < 1.3$) is taken to be the coincidence criterion [41], the simulation accuracy can be defined as the ratio of the number of such coincidences to the number of the comparison events. The 30% level meets the accuracy requirements of cross sections for nuclide production to be used in designing ADS plants, according to [41]. The mean simulated-to-experimental data ratio can be used as another coincidence criterion [6]:

$$\langle F \rangle = 10 \sqrt{\langle \log(\sigma_{cal,i}/\sigma_{exp,i})^2 \rangle}, \quad (36)$$

with its standard deviation

$$S(\langle F \rangle) = \langle (\log(\sigma_{cal,i}/\sigma_{exp,i}) - \log(\langle F \rangle))^2 \rangle, \quad (37)$$

where $\langle \rangle$ designates averaging over all the experimental and simulated results used in the comparisons ($i = 1, \dots, N_S$).

The mean ratio $\langle F \rangle$ together with its standard deviation $S(\langle F \rangle)$ defines the interval $[\langle F \rangle / S(\langle F \rangle), \langle F \rangle \times S(\langle F \rangle)]$ that covers about 2/3 of the simulation-to-experiment ratios. A logarithmic scale is preferable when determining the factor $\langle F \rangle$ rather than a linear scale, because the simulation-experiment differences may be as high as a few orders of magnitude.

We apply the above two criteria together with our results shown in Figs. 6–9, to infer conclusions about the predictive power of a given code.

The default options were used in all of the simulation codes without modifying the codes to get optimal agreement with the data. All the calculations were made before any experimental results were obtained, except the results from CEM2k. With such an approach, our comparisons demonstrate the real predictive power, rather than the descriptive power of the codes.

VII. COMPARISON OF EXPERIMENT WITH SIMULATIONS

The results obtained with the codes are presented in

- Fig. 6, which shows the results of a detailed comparison between simulated and experimental independent and cumulative products (criterion 1);
- Fig. 7, which shows the results of a detailed comparison between simulated and experimental independent products of all isotopes of Tm, Ir, and Tl measured in this experiment (black squares) together with the data obtained by the reverse-kinematics method at GSI (black stars) [8];
- Fig. 8, which shows the statistics of the simulated-to-experimental data ratios (criterion 2);
- Fig. 9, which shows the simulated mass distributions of the products together with the measured cumulative and supra cumulative yields of nuclides that are in immediate proximity to the stable isotope of a given mass (the sum of such yields from either side in cases when both left- and right-hand branches of the chain are present). Obviously, the simulation results do not contradict the experimental data if calculated values run above the experimental data and follow a general trend of the latter. This is because direct γ spectrometry identifies only the radioactive products, which generally form a significant fraction of the total mass yield but are

never equal to the total mass yield when a stable isobar is produced.

Table III presents quantitative information concerning the agreement of the simulated yields with experimental data for each of the simulation codes, namely:

- the total number of measured yields, N_T ;
- of them, the number of the measured yields selected to compare with calculations, N_G . We reject the following nuclides from our comparison in the cases where:
 1. The measured product is of metastable or just ground state, namely, ^{204m}Pb , ^{197m}Pb , $^{198m1}\text{Tl}$, ^{196m}Tl , ^{197m}Hg , ^{195m}Hg , ^{193m}Hg , ^{198m}Au , ^{198g}Au , ^{186g}Ir , ^{183m}Os , ^{182m}Re , ^{121m}Te , ^{119m}Te , ^{120m}Sb , ^{114m}In , ^{110m}Ag , ^{106m}Ag , ^{101m}Rh , ^{90m}Y , and ^{82m}Rb ;
 2. There is a transition of a metastable state to a product out of the given decay chain, namely, ^{198}Tl , ^{190}Ir , ^{152}Tb , ^{149}Gd , ^{121}Te , ^{96}Tc , ^{95}Tc , ^{95}Nb , ^{95}Nb , ^{89}Zr , ^{87}Y , and ^{85}Sr ;
 3. There is a strong correlation between a measured cumulative yield decaying into another one, namely, $^{173}\text{Ta} \rightarrow ^{173}\text{Hg}$, $^{170}\text{Hf} \rightarrow ^{170}\text{Lu}$, $^{169}\text{Lu} \rightarrow ^{169}\text{Yb}$, and $^{153}\text{Tb} \rightarrow ^{153}\text{Gd}$. The cumulative yields of the precursors in all the above chains are almost equal to the cumulative yields of the daughters, that is why only the daughter yields were used in our comparison, to prevent double counting. Also, in case of a strong correlation between the cumulative and independent yields of a product (^{88}Y), only the independent yield was used for comparison.
- of them, the number of the product nuclei whose yields were simulated by a particular code, N_S ;
- the number of comparison events when the simulated results differ from the experimental data by not more than 30%, $N_{C1.3}$, and the number of comparison events when the calculations differ from data by not more than a factor of 2.0, $N_{C2.0}$;
- the mean squared deviation of the simulated results from experimental data, $\langle F \rangle$, and its standard deviation, $S(\langle F \rangle)$.

Since about a third of all secondary nuclei from our reaction are not spallation products, the ability of codes to simulate high-energy fission processes is an important criterion for their ability to work when the target is heavy enough to fission. Among the codes used here, LAHET,

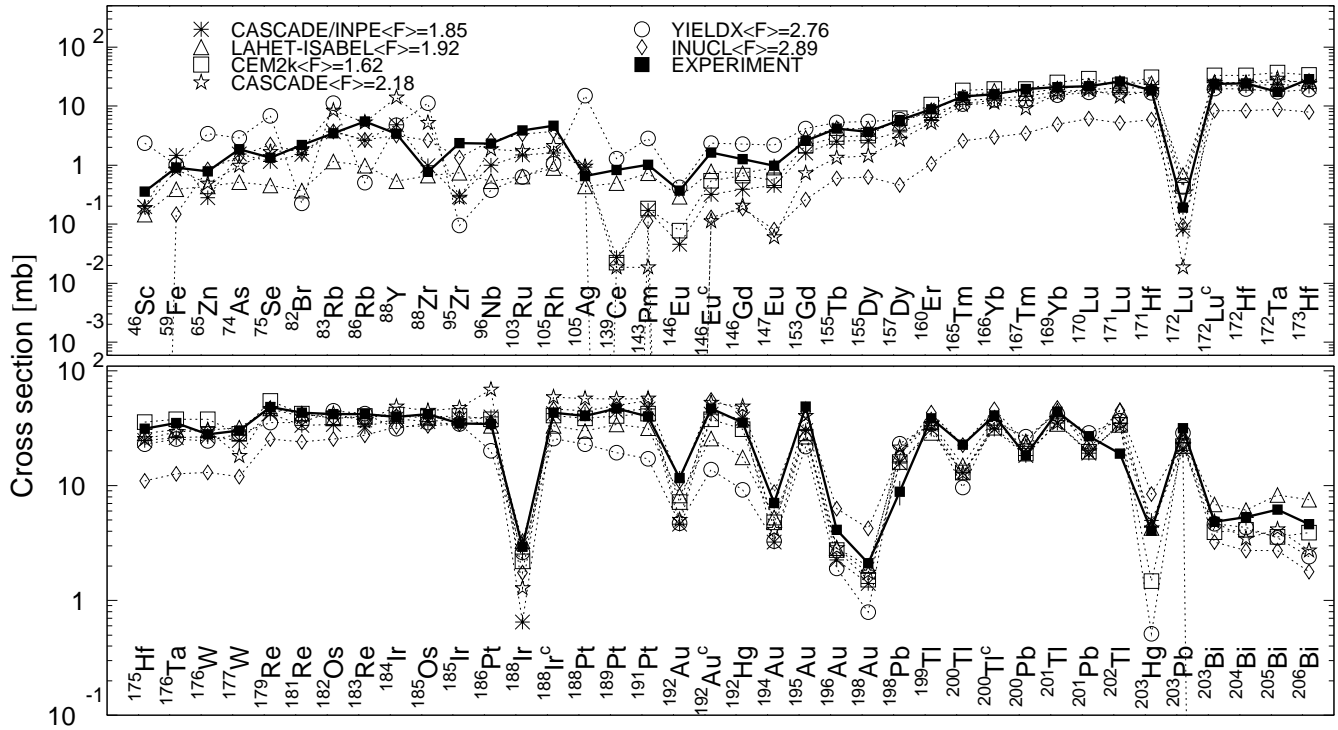


FIG. 6. Detailed comparison between experimental and simulated yields of radioactive reaction products. The cumulative yields are labeled with a “c” when the respective independent yields are also shown.

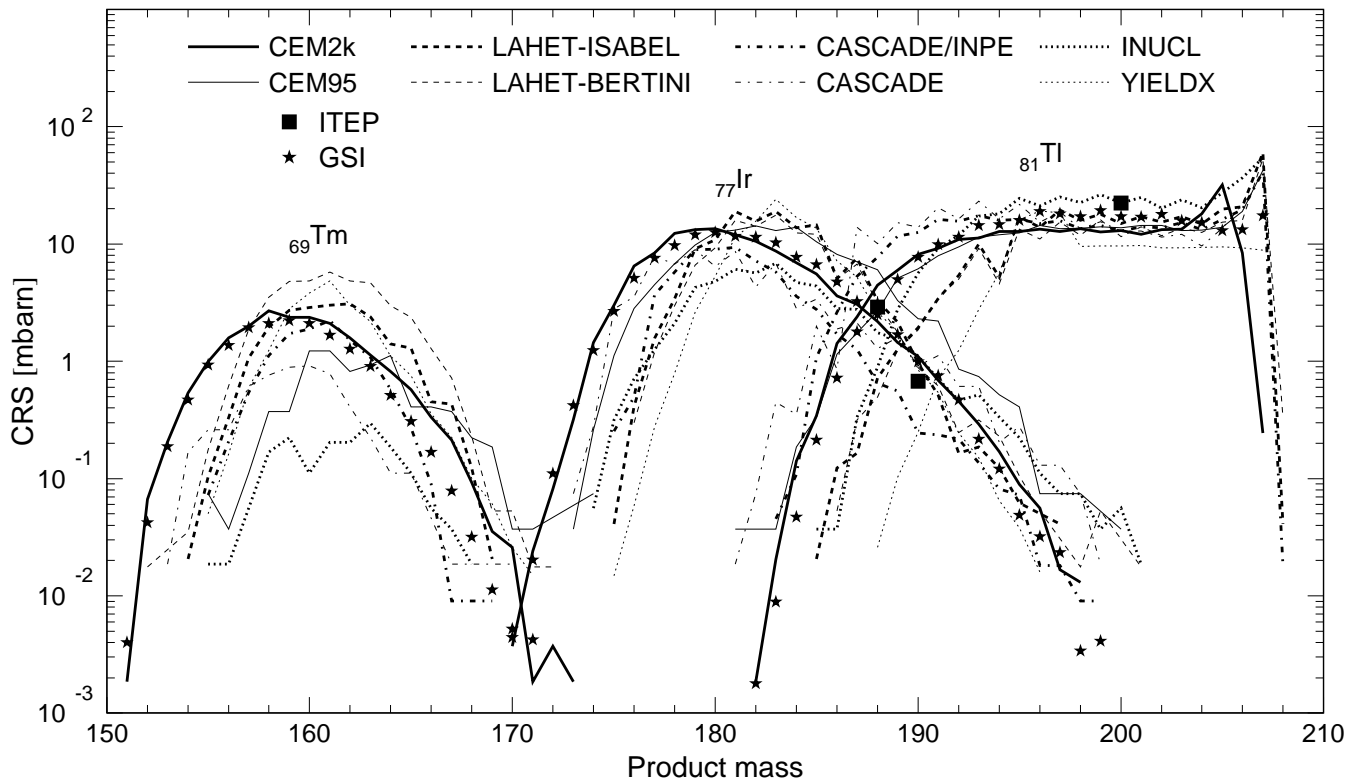


FIG. 7. Isotopic mass distribution for independent products of Tm, Ir, and Tl isotopes. Black squares are our measurements, while filled stars show GSI data obtained in reverse kinematics. Results from different codes are marked as indicated.

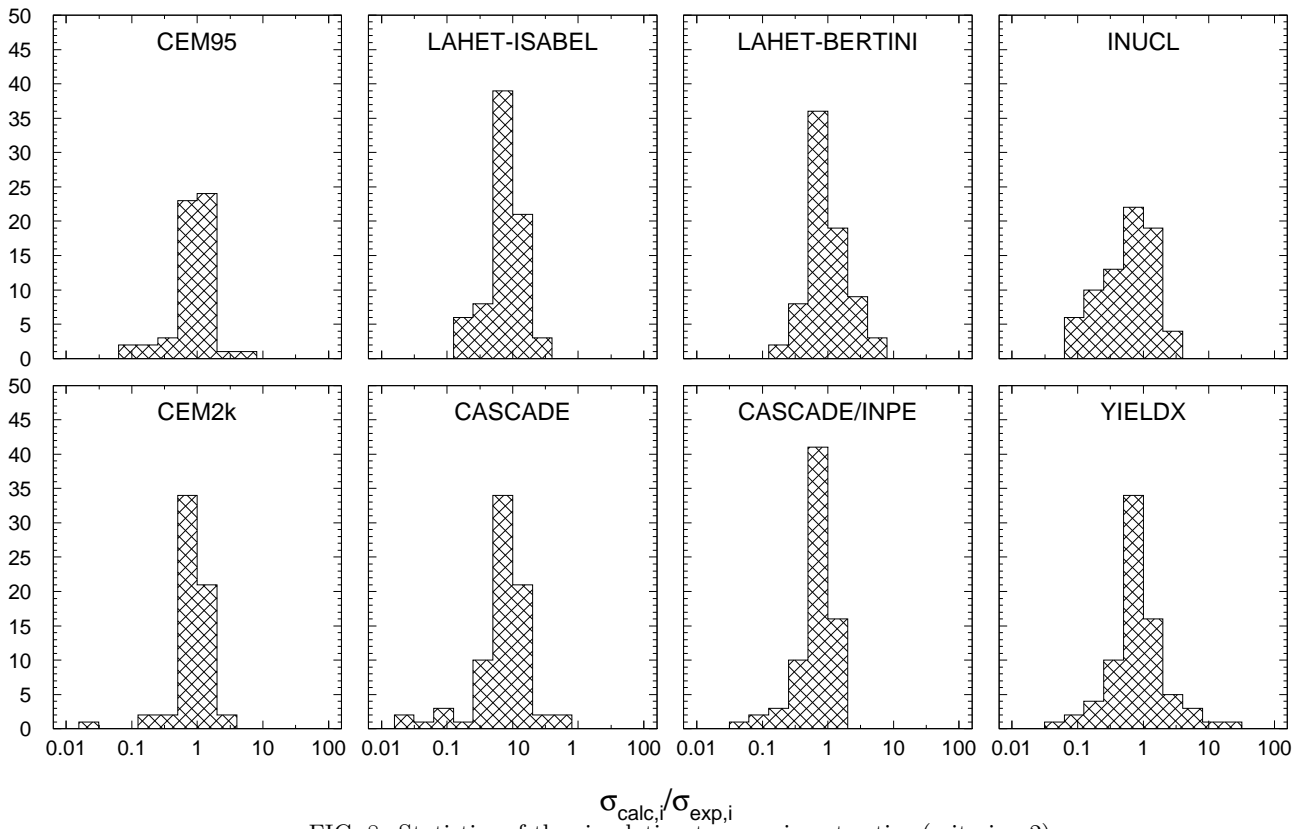


FIG. 8. Statistics of the simulation-to-experiment ratios (criterion 2).

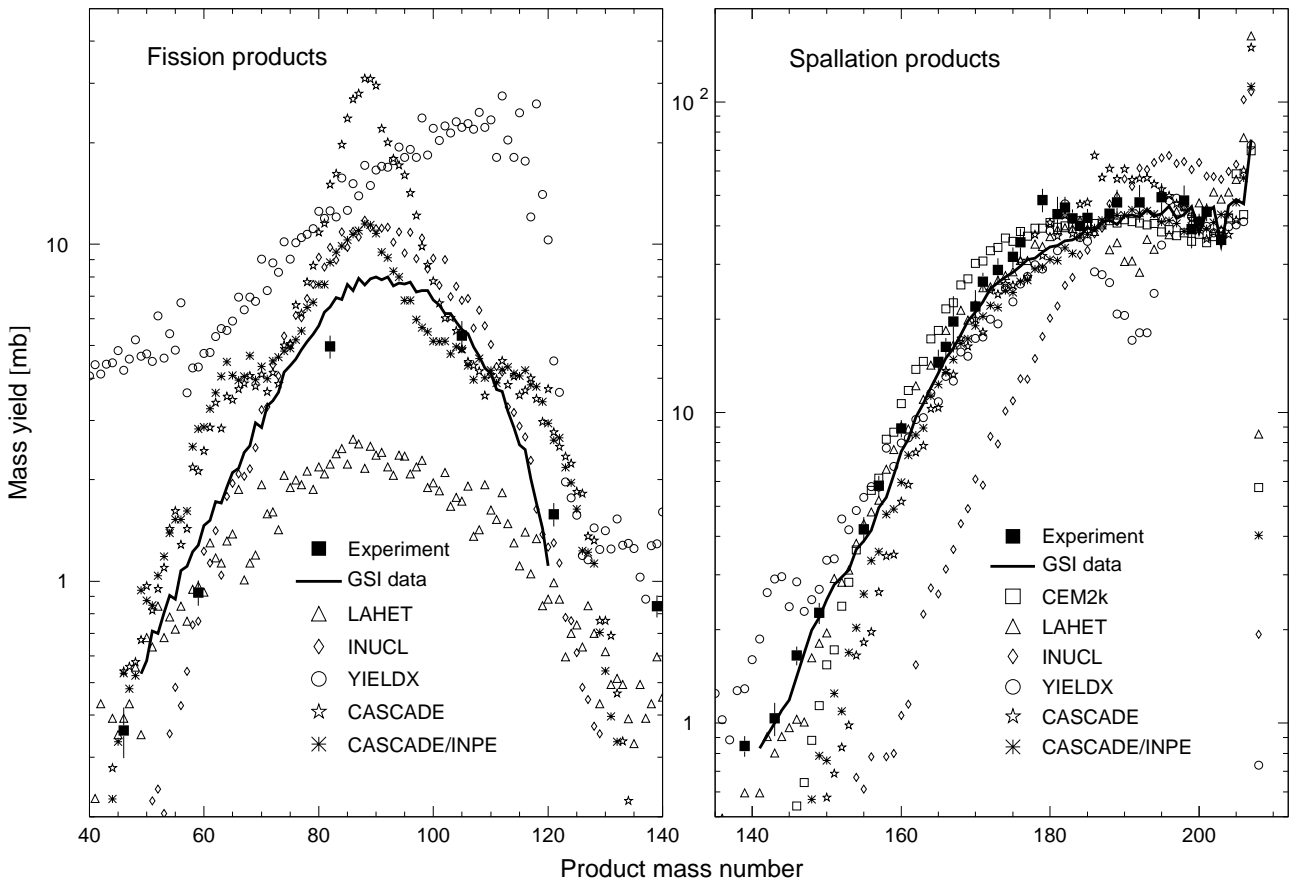


FIG. 9. The simulated mass distributions of reaction products together with the measured cumulative and supra-cumulative yields. Black line shows GSI data in reverse kinematics.

TABLE III. Statistics of comparison between experimental and simulated yields in 1.0 GeV proton-irradiated ^{208}Pb

Code	$N_T = 114, N_G = 76$		
	$N_{C_{1.3}} / N_{C_{2.0}} / N_S$	$\langle F \rangle$	$S(\langle F \rangle)$
LAHET-ISABEL	39/59/76	1.92	1.73
LAHET-Bertini	33/54/76	2.04	1.71
CEM95	30/46/55	2.16	2.00
CASCADE	29/55/72	2.18	1.88
CASCADE/INPE	32/56/70	1.85	1.59
INUCL	24/40/73	2.89	2.15
YIELDX	27/49/76	2.76	2.24
CEM2k	33/54/60	1.62	1.45

CASCADE, INUCL, CASCADE/INPE, and YIELDX simulate both spallation and fission products. The CEM95 and CEM2k codes simulate spallation only and do not calculate the process of fission, and do not provide fission fragments and a further possible evaporation of particles from them. When, during a Monte Carlo simulation of the compound stage of a reaction these codes encounter a fission, they simply remember this event (that permits them to calculate fission cross section and fissility) and finish the calculation of this event without a subsequent calculation of fission fragments. Therefore, results from CEM95 and CEM2k shown here reflect the contribution to the total yields of the nuclides only from deep spallation processes of successive emission of particles from the target, but do not contain fission products. This is explicitly reflected in a smaller number of the products simulated (the quantity N_S in Table III and in the shapes of the simulation curves in Figs. 6 and 9). To be able to describe nuclide production in the fission region, these codes have to be extended by incorporating a model of high energy fission (e.g., in the transport code MCNPX [42], where CEM97 is used, it is supplemented by the RAL fission model [43]).

The following conclusions follow from the analysis of the results presented in Table III and in Figs. 6–9:

1. All codes can reasonably adequately simulate the weak spallation reactions (the $A > 180$ products), with simulation results differing from experimental data, usually within a factor of 2. The exceptions are the yields of ^{203}Hg (underestimated by an order of magnitude by YIELDX) and ^{188}Ir (underestimated by an order of magnitude by CASCADE/INPE). It should be noted that all the codes simulate a number of products (^{184}Ir , ^{198}Tl , ^{199}Tl , $^{200}\text{Tl}(\text{cum})$, ^{201}Tl , and ^{203}Pb), which differ from experiment by less than 30%.
2. In the range of the deep spallation reactions ($150 < A < 180$), the simulation codes have very dif-

ferent predictive powers, namely,

- the LAHET, CASCADE/INPE, and YIELDX predictions are very close to the experimental data; the only exception is $^{172}\text{Lu}(\text{ind})$, whose measured yield is about a factor of two smaller than LAHET and YIELDX give and about a factor of two higher than the CASCADE/INPE prediction;
 - the CASCADE code simulates the $A > 160$ product yields quite adequately, except for $^{172}\text{Lu}(\text{ind})$ whose measured yield is about ten times above the simulated value; however, as the atomic number of the product decreases below 160, we observe an underestimation of data by CASCADE; the deviation tends to increase with decreasing A (up to a factor of 5);
 - the INUCL code underestimates these reaction products systematically by a factor of 2–10 with the discrepancy increasing with decreasing A ;
 - the new code CEM2k was developed taking into account the recent GSI measurements [8]. In the spallation region it agrees best with the data compared to all the other codes, although like its predecessor CEM95, it does not contain explicit treatment of fission fragments and should be supplemented in a transport code by a model of fission-fragment formation, or should be improved further by the development and incorporation of its own model of fission-fragment formation.
3. In the range of fission products ($40 < A < 150$), the INUCL code predictions are in the best agreement with the data. As a rule, the INUCL-simulated yields differ from measured data by a factor of less than 1.5, except for ^{59}Fe , ^{139}Ce , and ^{143}Pm . The LAHET-simulated yields underestimate data by a factor of 1.5–10, except for ^{88}Zr and ^{105}Ag . The specific predictions of isotope production cross sections (Fig. 6) of the semi-phenomenological code YIELDX both under- and overestimate the fission product data by a factor of up to 30, without showing any obvious patterns in the disagreement. In contrast, the YIELDX isobar cross sections are all greatly overpredicted, as shown in Fig. 9. The CASCADE/INPE-simulated yields of the $130 < A < 150$ products are strongly underestimated (up to 1–2 orders of magnitude), while the rest of the simulated fission product yields agree with the experimental data generally within a factor of 2. As a rule, the agreement of all codes with the data in the fission product region is worse than in the spallation region; therefore, development of a better model for fission-fragment formation is welcomed for any code.

VIII. CONCLUSION

The interest shown in both the possible transmutation of nuclear wastes and the Spallation Neutron Source (SNS) facilities encourage us to anticipate that the accumulation and analysis of nuclear data for ADS and SNS applications will have the same growth in academic interest and practical commitments as was the case for nuclear reactor data during the last five decades. Therefore, experimental data on the yields of proton-induced reaction products as applied to the ADS and SNS main target and structure materials are of great interest and importance. It should be emphasized that the charge distributions in the isobaric decay chains are important as well. The information thus obtained would make it possible, first, to raise the information content of the comparisons between experimental and simulated data and, second, to reduce the uncertainties in experimental determination of the cumulative yields by establishing unambiguous relations between σ^{cum} and σ^{cum*} for many of the reaction products.

We have measured in the present work 114 cross sections of nuclides produced in interactions of 1 GeV protons with ^{208}Pb , of which 8 are independent yields of ground states, 15 are independent yields of metastable states, 15 are independent yields of metastable and ground states, 65 are cumulative yields, and 11 are supra cumulative yields. We have compared our data with previous measurements and with predictions of seven different codes used in many current applications to understand qualitatively and to estimate quantitatively their predictive powers.

Regarding the codes benchmarked here, we conclude that none of them agree well with the data in the whole mass region of product nuclides and all should be improved further. In addition, the predictive power of all codes for data in the fission product region is worse than in the spallation region; therefore, development of better models for fission-fragment formation is of first priority. The new CEM2k code developed recently at Los Alamos [32] motivated by the recent GSI data [8] agrees best with our data in the spallation region, of the codes tested. But CEM2k is inapplicable in the fission-product region, as to date it has no model of fission-fragment formation.

ACKNOWLEDGMENTS

The authors are indebted to Drs. T. Enqvist and B. Mustapha for providing us the cross sections measured at the GSI, to Prof. R. Michel for sending us the nuclide production data obtained at the ZSR, to Dr. F. E. Chukreev for helpful comments on the nuclear decay-chain data, and to Prof. V. Artisyuk for useful discussions and help.

The work has been performed under the ISTC Project #839 supported by the European Community, Japan

(JAERI), and Norway and was partially supported by the U. S. Department of Energy.

-
- [1] G. J. Van Tuyle, "ATW Technology Development & Demonstration Plan", Los Alamos National Laboratory Report No. LA-UR-99-1061, Los Alamos, 1999; "ATW Technology & Scenarios", Los Alamos National Laboratory Report No. LA-UR-99-771, Los Alamos, 1999.
 - [2] T. Mukaiyama, in *Proceedings of the Third International Conference on Accelerator-Driven Transmutation Technologies and Applications (ADTT'99)*, Praha, Czech Republic, 1999, paper Mo-I-5 on the conference CD-ROM and Web page http://fjfi.cvut.cz/con_adtt99.
 - [3] M. Salvatores, in *Proceedings of the Third International Conference on Accelerator-Driven Transmutation Technologies and Applications (ADTT'99)*, Praha, Czech Republic, 1999, paper Mo-I-4 on the conference CD-ROM and Web page http://fjfi.cvut.cz/con_adtt99.
 - [4] Yu. V. Alexandrov, V. P. Eismont, R. V. Ivanov, M. A. Mikhailova, V. P. Prikhodtseva, A. V. Saulsky, and S. K. Vasiljiev, in *Proceedings of the Second International Conference on Accelerator-Driven Transmutation Technologies and Applications (ADTT'96)*, Kalmar, Sweden, 1996, edited by H. Conde (Uppsala University, Uppsala, 1997), p. 576.
 - [5] M. Gloris, R. Michel, U. Herpers, F. Sudbrok, and D. Filges, *Nucl. Instrum. Methods B* **113**, 429 (1996).
 - [6] Yu. E. Titarenko, O. V. Shvedov, M. M. Igumnov, S. G. Mashnik, E. I. Karpikhin, V. D. Kazaritsky, V. F. Batyaev, A. B. Koldobsky, V. M. Zhivun, A. N. Sosnin, R. E. Prael, M. B. Chadwick, T. A. Gabriel, and M. Blann, *Nucl. Instrum. Methods A* **414**, 73 (1998).
 - [7] R. Michel, M. Gloris, H.-J. Lange, I. Leya, M. Luepke, U. Herpers, B. Dittrich-Hannen, R. Roesel, Th. Schiekel, D. Filges, P. Dragovitsch, M. Suter, H.-J. Hofmann, W. Wölfl, P. W. Kubik, H. Baur, and R. Wieler, *Nucl. Instrum. Methods B* **103**, 183 (1995).
 - [8] W. Wlazlo, T. Enqvist, P. Armbruster, J. Benlliure, M. Bernas, A. Boudard, S. Czajkowski, R. Legrain, S. Leray, B. Mustapha, M. Pravikoff, F. Rejmund, K.-H. Schmidt, C. Stéphan, J. Taieb, L. Tassan-Got, and C. Volant, *Phys. Rev. Lett.* **84**, 5736 (2000); T. Enqvist, W. Wlazlo, P. Armbruster, J. Benlliure, M. Bernas, A. Boudard, S. Czajkowski, R. Legrain, S. Leray, B. Mustapha, M. Pravikoff, F. Rejmund, K.-H. Schmidt, C. Stéphan, J. Taieb, L. Tassan-Got, and C. Volant, "Isotopic Yields and Kinematic Energies of Primary Residues in 1A GeV $^{208}\text{Pb} + p$ Reactions," GSI Preprint 2000-28, submitted to *Nucl. Phys. A*.
 - [9] W. Wlazlo, T. Enqvist, P. Armbruster, J. Benlliure, M. Bernas, A. Boudard, S. Czajkowski, F. Farget, R. Legrain, S. Leray, B. Mustapha, M. Pravikoff, K.-H. Schmidt, C. Stéphan, J. Taieb, L. Tassan-Got, and C. Volant, "Isotope Production in 1 · A GeV ^{208}Pb on Proton Reactions," in *Proceedings of the Third Interna-*

- tional Conference on Accelerator-Driven Transmutation Technologies and Applications (ADTT'99), Praha, Czech Republic, 1999*, paper Mo-O-C2 on the conference CD-ROM and Web page http://fjfi.cvut.cz/con_adtt99.
- [10] L. Tassan-Got, B. Mustapha, F. Farget, M. Bernas, C. Stéphan, P. Armbruster, J. Benlliure, T. Enqvist, K.-H. Schmidt, A. Boudard, R. Legrain, S. Leray, C. Volant, W. Wlazlo, S. Czajkowski, and M. Pravikoff, "Spallation Residue Cross-Sections in Reverse Kinematics," in *Proceedings of the International Conference on the Physics of Nuclear Science and Technology*, Long Beach, New York, 1998 (ANS, La Grange Park, IL, 1998), vol. 2, p. 1334.
- [11] R. W. Mills, M. F. James, and D. R. Weaver, "The JEF2 Fission Product Yields Evaluation", in *Proceedings of a Specialists' Meeting on Fission Product Nuclear Data, Tokai, Japan, 1992*, p.358; NEA/NSC/DOC(92)9.
- [12] U. Reus and W. Westmeier, *Atomic Data and Nuclear Data Tables* **29**, 1 (1983).
- [13] International Science and Technology Center (ISTC) Contract 839-2, see the web page at: <http://www.istc.ru>.
- [14] A. Yu. Konobeev, A. Yu. Korovin, P. E. Pereslavitsev, V. I. Plyaskin, and A. Yu. Stankovsky, International Atomic Energy Agency Report No. INDC(CCP)-384, Vienna, 1995.
- [15] V. P. Eismont, A. I. Obukhov, A. V. Prokofiev, and A. N. Smirnov, in *Proceedings of the Second International Conference on Accelerator-Driven Transmutation Technologies and Applications (ADTT'96), Kalmar, Sweden, 1996*, edited by H. Conde (Uppsala University, Uppsala, 1997), p. 592.
- [16] Yu. N. Shubin, V. P. Lunev, A. Yu. Korovin, and A. I. Dityuk, International Atomic Energy Agency Report No. IC(CCP)-385, Vienna, 1995.
- [17] J. Tobailem, "Sections Efficaces des Reactions Nucleaires Induites par Protons, Deutrons, Particules Alphas. V. Silicium," Note CEA-N-1466(5), Sacley, 1981.
- [18] R. Michel, F. Peiffer, and R. Stück, *Nucl. Phys.* **A441**, 617 (1985).
- [19] R. Michel, P. Dragovitsch, P. Englert, F. Peiffer, R. Stück, S. Theis, F. Begemann, H. Weber, P. Signer, R. Wieler, D. Filges, and P. Cloth, *Nucl. Instrum. Methods B* **16**, 61 (1986).
- [20] R. Michel, B. Dittrich, U. Herpers, F. Peiffer, T. Schiffmann, P. Cloth, P. Dragovitsch, and D. Filges, *Anayst* **114**, 287 (1989).
- [21] B. Dittrich, U. Herpers, M. Lüpke, R. Michel, P. Signer, R. Wieler, H. J. Hofmann, and W. Wölfl, in: Progress Report on Nuclear Data Research in the Federal Republic of Germany for the Period April 1, 1989 to March 31, 1990, NEANDC(E)-312-U Vol. V INDC(Ger)-35/LN+Special (1990), p. 45.
- [22] R. Bodemann, H.-J. Lange, I. Leya, R. Michel, T. Schiekel, R. Rösel, U. Herpers, H. J. Hofmann, B. Dittrich, M. Suter, W. Wölfl, B. Holmqvist, H. Condé, and P. Malmberg, in: Progress Report on Nuclear Data Research in the Federal Republic of Germany for the Period April 1, 1992 to March 31, 1993, NEA/NDC/DOC(93) 17, INDC(Ger)-037/LN. Jul-2803 (1993), p. 49.
- [23] Th. Sciekel, F. Sudbrock, U. Herpers, M. Gloris, H.-J. Lange, I. Leya, R. Michel, B. Dittrich-Hannen, H.-A. Synai, M. Suter, P. W. Kubik, M. Blann, and D. Filges, *Nucl. Instrum. Methods B* **114**, 91 (1996).
- [24] R. Michel, R. Bodermann, H. Busemann, R. Daunke, M. Gloris, H.-J. Lange, B. Klug, A. Krins, I. Leya, M. Lüpke, S. Neumann, H. Reinhardt, M. Schnatz-Büttgen, U. Herpers, Th. Sciekel, F. Sudbrock, B. Holmqvist, H. Condé, P. Malmberg, M. Suter, B. Dittrich-Hannen, P. W. Kubik, H.-A. Synai, and D. Filges, *Nucl. Instrum. Methods B* **129**, 153 (1997).
- [25] Model S502 Genie-2000 Basic Spectroscopy Software. V1.X Russian; Model S561 Genie-2000 Batch Programming Support. V1.1.
- [26] R. R. Kinsey et al., Proc. 9th Int. Symp. of Capture-Gamma-Ray Spectroscopy and Related Topics, 8-12 October 1996, Budapest, Hungary, in press; <http://www.fysik.lu.se/nucleardata/cdrom/pcnudat.htm>.
- [27] R. B. Firestone, in: *Tables of Isotopes, 8th ed.: 1998 Update (with CD ROM)* edited by S. Y. Frank Chu (CD-ROM Ed.), C. M. Baglin (Ed.), (Wiley Interscience, New York, 1996).
- [28] D. J. Hudson, *Statistics Lectures on Elementary Statistics and Probability* (Geneva, 1964).
- [29] M. Gloris, R. Michel, F. Sudbrock, U. Herpers, P. Malmberg, B. Holmqvist, "Proton-Induced Production of Residual Radionuclides in Lead at Intermediate Energies," to be published in *Nucl. Instrum. Methods A* (2000).
- [30] K. K. Gudima, S. G. Mashnik, and V. D. Toneev, *Nucl. Phys. A* **401**, 329 (1983); S. G. Mashnik, "User Manual for the Code CEM95", JINR, Dubna, 1995; OECD Nuclear Energy Agency Data Bank, Paris, France, 1995; <http://www.nea.fr/abs/html/iaea1247.html>; RSIC-PSR-357, Oak Ridge, 1995.
- [31] S. G. Mashnik and A. J. Sierk, in *Proceedings of the Fourth International Workshop on Simulating Accelerator Radiation Environments (SARE4), Knoxville, TN, 1998*, edited by T. A. Gabriel, (ORNL, 1999), p. 29.
- [32] S. G. Mashnik and A. J. Sierk, "CEM2k - Recent Developments in CEM," Los Alamos National Laboratory Report LA-UR-00-5437 (2000); <http://xxx.lanl.gov/ps/nucl-th/001164>; to be published in *Proceedings of the Fourth International Topical Meeting on Nuclear Applications of Accelerator Technology (AccApp00), November 13-15, 2000, Washington, DC, USA*.
- [33] V. S. Barashenkov, Le Van Ngok, L. G. Levchuk, Zh. Zh. Musul'manbekov, A. N. Sosnin, V. D. Toneev, and S. Yu. Shmakov, JINR Report R2-85-173, Dubna, 1985; V. S. Barashenkov, F. G. Zheregi, and Zh. Zh. Musul'manbekov, *Yad. Fiz.* **39**, 1133 (1984) [*Sov. J. Nucl. Phys.* **39**, 715 (1984)]; V. S. Barashenkov, B. F. Kostenko, and A. M. Zadorogny, *Nucl. Phys. A* **338**, 413 (1980).
- [34] G. A. Lobov, N. V. Stepanov, A. A. Sibirtsev, and Yu. V. Trebukhovskii, Institute for Theoretical and Experimental Physics (ITEP) Preprint No. ITEP-91, Moscow, 1983; A. A. Sibirtsev, N. V. Stepanov, and Yu. V. Trebukhovskii, ITEP Preprint No. ITEP-129, Moscow, 1985; N. V. Stepanov, ITEP Preprint No. ITEP-

- 81, Moscow, 1987; N. V. Stepanov, ITEP Preprint No. ITEP-55-88, Moscow, 1988 (in Russian).
- [35] R. E. Prael and H. Lichtenstein, "User guide to LCS: The LAHET Code System," Los Alamos National Laboratory Report No. LA-UR-89-3014 (1989); see also the Web page at: <http://www-xdiv.lanl.gov/XTM/lcs/lahet-doc.html>.
- [36] C. H. Tsao, Private communication; R. Silberberg, C. H. Tsao, and A. F. Barghouty, *Astrophys. J.*, **501**, 911 (1998); R. Silberberg and C. H. Tsao, *Astrophys. J. Suppl.*, No. 220, **25**, 315 (1973); *ibid.*, p. 335.
- [37] V. S. Barashenkov, A. Yu. Konobeev, Yu. A. Korovin, and V. N. Sosnin, *Atomnaya Energiya* **87**, 283 (1999) [*Atomic Energy* **87**, 742 (1999)].
- [38] V. S. Barashenkov and V. D. Toneev, *Interactions of High-Energy Particles and Atomic Nuclei with Nuclei* [in Russian] (Atomizdat, Moscow, 1972).
- [39] G. Audi and A. H. Wapstra, *Nucl. Phys. A* **595**, 409 (1995).
- [40] J. R. Letaw, R. Silberberg, and C. H. Tsao, *Astrophys. J. Suppl.*, **51**, 271 (1983).
- [41] A. Koning, in *Proceedings of the Second International Conference on Accelerator-Driven Transmutation Technologies and Applications (ADTT'96), Kalmar, Sweden, 1996*, edited by H. Conde (Uppsala University, Uppsala, 1997), p. 438.
- [42] *MCNPXTM User's Manual, Version 2.1.5*, edited by Laurie S. Waters, Los Alamos National Laboratory Report LA-UR-99-6058 (1999).
- [43] F. Atchison, "Spallation and Fission in Heavy Metal Nuclei under Medium Energy Proton Bombardment," in *Targets for Neutron Beam Spallation Source*, Jul-Conf-34, Kernforschungsanlage Julich GmbH (January 1980).